UNIVERSITÀ
DEGLI STUDI
FIRENZE

DOTTORATO DI RICERCA IN ENERGETICA E
TECNOLOGIE INDUSTRIALI E AMBIENTALI INNOVATIVE

CICLO XXXIII
COORDINATORE Prof. Giampaolo Manfrida

TOWARDS THE ADVANCED MODELLING OF THE LOW PRESSURE STAGES OF THE STEAM TURBINES

Settore scientifico disciplinare ING-IND/08

Ph.D. Candidate
Eng. Nicola Maceli

Tutor
Prof. Andrea Arnone

Coordinatore
Prof. Giampaolo Manfrida

Firenze, 2017/2020

UNIVERSITÀ
DEGLI STUDI
FIRENZE

DOTTORATO DI RICERCA IN ENERGETICA E
TECNOLOGIE INDUSTRIALI E AMBIENTALI INNOVATIVE

CICLO XXXIII
COORDINATORE Prof. Giampaolo Manfrida

TOWARDS THE ADVANCED MODELLING OF THE LOW PRESSURE STAGES OF THE STEAM TURBINES

Settore scientifico disciplinare ING-IND/08

Ph.D. Candidate
Eng. Nicola Maceli
Department of Industrial Engineering, University of Florence
Nuovo Pignone, Baker Hughes Company, Florence

Tutor
Prof. Andrea Arnone
Department of Industrial Engineering, University of Florence

Firenze, 2017/2020

... in order to progress we must recognize our ignorance and leave room for doubt. Scientific knowledge is a body of statements of varying degrees of certainty — some most unsure, some nearly sure, but none absolutely certain.

From: *The value of science*, 1955, Richard P. Feynman

To my beloved Sakiko and Luca.
All I did is for you, I did nothing without you.

Acknowledgments

I look back and realize how lucky I am for the opportunity I had to spend the last three years studying a subject that filled me with passion. Thanks to all the friends that cheered me up and helped me smile even when everything seemed so hard. I am indebted with my Ph.D Tutor Prof. Andrea Arnone for trusting me and supporting me in this research. I'll always be grateful to Baker Hughes Nuovo Pignone for letting me publish all the material presented in this thesis and for the financial support. I'll be forever in debt to my colleagues and managers at Baker Hughes Nuovo Pignone Lorenzo Cosi and Lorenzo Arcangeli, for they encouraged me to start this long adventure.

Abstract

The development of new steam turbines with higher efficiency, better operability, and reduced costs is still of current interest in the energy market. To this purpose, the prediction tools need to be able to account for all the geometrical details and all the physical effects that are relevant for the performance. Furthermore, they are required to provide the designers with the pieces of information that they need to evaluate the severity of the damage caused to the rotating blades by the coarse water present in the large droplets detaching from the trailing edge of the stationary vanes. In the current industrial approach, the validation of new LP sections is done with a combination of standard CFD and correlative methodologies followed by a significant experimental activity. The recent development of solvers for two-phase flows capable to model in details the geometry of the blading and of the sealing could give a powerful tool for the screening of new designs and the performance estimation. However, as shown by recent publications on this subject, the theory behind these computational methodologies is still affected by significant uncertainty. As a result, no common modelling approach exists in the industrial practice. A stimulating debate is on-going to consolidate the nucleation theory and the equations used to model the growth of the water droplets. This research project aims to

promote the CFD methodology from being a tool for qualitative analyses to quantitative predictions. In order to do so, a set of user defined functions has been coded to be used together with a commercial code. To improve its predictive capability, different modeling hypotheses and parameters have been considered and tested on different configurations, spanning from plane nozzles to turbine cascade to a complete LP section. Different steam conditions have been considered too, so that the losses due to the nucleation and the droplets growth are put in evidence.

Contents

Contents viii

List of Figures xii

List of Tables xiii

Nomenclature xv

1 Introduction 1

2 The theoretical framework 7

2.1 Physical Models 8

2.1.1 The droplet nucleation 8

2.1.2 The droplet growth 13

2.2 Loss Models 19

2.2.1 The nucleation losses 19

2.2.2 The thermodynamic relaxation losses . . . 20

2.2.3 The Bauman factor 24

2.2.4 The kinetic energy losses 27

3 The numerical methodology 31

3.1 The two-phase flow equations 32

3.1.1 An introduction 32

3.1.2 The CFD equations 36

4 Plane nozzle analysis **41**
4.1 Analysis of plane nozzles 42
4.1.1 The Moses and Stein plane nozzle 42
4.1.2 The Binnie and Green plane nozzle 49

5 Cascade Analysis **53**
5.1 The Bakhtar cascade 54
5.1.1 The cases with nucleating steam 55
5.1.2 The cases with wet steam 63
5.2 Comparison with correlations 66

6 Analysis of a LP section **75**
6.1 The Low-Pressure section 76
6.2 The test rig layout 77
6.3 The numerical setup 80
6.4 The numerical results 83
6.4.1 Comparison to the test data 84
6.4.2 The wetness losses 91
6.4.3 Aerodynamic aspects 95
6.4.4 The comparison with the correlations . . 103
6.4.5 The kinetic energy losses 106

7 Conclusions **109**

References **113**

List of Figures

1.1 Low pressure stage design space 3

2.1 Free energy change in the formation of a droplet at 100^0C 11
2.2 Critical radius for different supersaturation conditions and vapour temperatures 11
2.3 Efficiency drop as a function of average wetness . 24
2.4 Thermal Reheat Factor for the considered test data 26
2.5 Polytropic efficiency drop as a function of average wetness 26
2.6 Efficiency drop with dry endpoint 27

4.1 The geometry of the Moses and Stein plane nozzle 42
4.2 The computational mesh of the Moses and Stein plane nozzle 43
4.3 The pressure distribution for the Moses and Stein plane nozzle 44
4.4 Detail of the Pressure ratio distribution for the Moses and Stein plane nozzle 45
4.5 Droplet diameter distribution for the Moses and Stein case: Equation 2.29 46

4.6 The droplet diameter distribution for the Moses and Stein case: Equation 2.39 46
4.7 The pressure distribution for the Moses and Stein case: Equation 2.29 and Equation 2.39 results . . 47
4.8 The nucleation rate J_{NI} for the Moses and Stein plane nozzle 48
4.9 The supercooling for the Moses and Stein plane nozzle 48
4.10 The geometry of the Binnie and Green plane nozzle 49
4.11 The computational mesh of the Binnie and Green plane nozzle 50
4.12 The pressure distribution of the Binnie and Green plane nozzle 52
4.13 The pressure gradient of the Binnie and Green plane nozzle 52

5.1 Mesh blocking 54
5.2 Grid sensitivity study (TP27, 1C14SEP9) 55
5.3 The details of the mesh used for the analysis of the Bakhtar cascade. 56
5.4 Superheated test: Surface Pressure (TP30, 4H15SEP9). 57
5.5 Nucleating test: Surface Pressure (TP27, 1C14SEP9). 58
5.6 Effects of the surface tension (TP27, 1C14SEP9). 58
5.7 Adjustment of the exit pressure (TP27, 1C14SEP9). 59
5.8 Effect of the mesh refinement (TP27, 1C14SEP9). 60
5.9 Effect of the tension correction on bladerow efficiency (TP27, 1C14SEP9). 60
5.10 Test and calculated data w/ and w/o correction. 61
5.11 Sensitivity to the parameters of Young Equation 2.39. 62
5.12 Comparison between numerical and test values: cases A and B 64

5.13 Comparison between numerical and test values: cases A and F 65
5.14 Comparison between numerical and test values: cases A and C 66
5.15 Efficiency drop vs average moisture. 67
5.16 Nucleation losses: comparison between numerical and theoretical estimates. 68
5.17 Supercooling for the 4% and 6% cases. 69
5.18 Nucleation rate for the 4% and 6% cases. 69
5.19 Wetness distribution and maximum supercooling for the 4% and 6% cases. 70
5.20 Thermodynamic relaxation losses: comparison between numerical and theoretical estimates. . . . 71
5.21 Expansion rate: case C. 72
5.22 Thermodynamic relaxation losses from Equation 2.54 at varying $\dot{P}$. 73

6.1 Test vehicle layout with instrumentation 78
6.2 Main characteristics of test facility 79
6.3 View of the computational domain. 83
6.4 Equilibrium Steam: Total-to-total efficiency vs PRts. 84
6.5 Non-Equilibrium Steam: Total-to-total efficiency vs PRts. 85
6.6 Radial distributions at the L1 stage inlet: G6 condition. 86
6.7 Radial distributions at the L0 stage inlet: G6 condition. 86
6.8 Radial distributions at the L0 stage exit: G6 condition. 88
6.9 Parity plot of total-to-total efficiency. 89
6.10 Parity plot of wetness losses. 91

6.11 Efficiency drop at different exhaust moisture. . . 93
6.12 Expansion lines of the considered cases. 94
6.13 Reheat factor for the considered cases. 94
6.14 Supercooling for the B6 test point. 96
6.15 Supercooling for the D4 test point. 96
6.16 Nucleation region for the B6 test point. 97
6.17 Nucleation region for the D4 test point. 97
6.18 Stage Pressure ratio for different test points: ES results. 99
6.19 Load coefficients for different test points: ES results. 99
6.20 Stage Pressure ratio for different test points: NES results. 100
6.21 Load coefficients for different test points: NES results. 101
6.22 Pressure distributions for L1 and L0 stages: B6 test point. 102
6.23 Pressure distributions for L1 and L0 stages: D4 test point. 102
6.24 Wetness losses: comparison between numerical and theoretical estimates. 104
6.25 Schematic of an expansion line. 105
6.26 Wetness losses: experiments and numerical estimates. 106
6.27 Leaving losses: difference between ES and NES results. 108
6.28 Radial distribution of the absolute velocity at the L0 Bucket exit. 108

List of Tables

2.1 Energy transfer range 13

3.1 Governing equations 39

4.1 Boundary conditions for test 96 51

5.1 Conditions for the analysis of the wet cases of the Bakhtar's cascade. 64

Nomenclature

Roman Letters

Symbol	Description	Units
$A_{exhaust}$	Annulus area at the exit of the LP section	$[\mathrm{m}^2]$
c_p	const. press. specific heat	$[\mathrm{J\,kg^{-1}\,K^{-1}}]$
F	Influence coefficient for $\dot{P}$ in Equation 2.48	$[-]$
G	Gibbs free energy	$[\mathrm{J\,kg^{-1}}]$
H	Enthalpy	$[\mathrm{J\,kg^{-1}}]$
J	Nucleation rate	$[\mathrm{m^{-3}\,s^{-1}}]$
k	Boltzmann constant	$[\mathrm{J\,K^{-1}}]$
Kn	Knudsen number	$[-]$
L	Latent heat	$[\mathrm{J\,kg^{-1}}]$
$\tilde{l}$	Mean free-path lenght	[m]
LL	Leaving losses or kinetic energy at the LP section exit	$[\mathrm{m^2\,s^{-2}}]$

$Loss_{bearing}$	Power lost due to the oil bearing	[W]
$\dot{m}$	Mass flow rate	[kg s^{-1}]
M	Mass of one droplet	[kg]
m	Mass of one water molecule	[kg]
$\dot{m}_d$	Mass transfer rate for phase d	[kg s^{-1}]
n	Number of embryos per unit volume	[m^{-3}]
Nu	Nusselt number	[−]
N_d	Droplets number per unit volume	[m^{-3}]
P	Pressure	[Pa]
$\dot{P}$	Expansion rate	[s^{-1}]
Pr	Prandtl number	[−]
$\dot{q}$	Heat flow	[W]
Q_c	Condensation coefficient	[−]
Q_e	Evaporation coefficient	[−]
R	Gas constant	[J kg^{-1} K^{-1}]
r	Droplet radius	[m]
Re	Reynolds number	[−]
RH	Thermal reheat factor	[−]
s	Specific entropy	[J kg^{-1} K^{-1}]
S	Generic term from two-phase flows equations in Table 3.1	[−]

T	Temperature	[K]
$\mathbb{T}$	Shaft torque	[N m]
t	Time	[s]
u	Velocity	[$\mathrm{m\,s^{-1}}$]
u_b	blade peripheral velocity at midspan	[$\mathrm{m\,s^{-1}}$]
u_x	Axial velocity	[$\mathrm{m\,s^{-1}}$]
We	Weber number	[–]
Y	Mass fraction of water present in the mixture	[–]

Greek Letters

Symbol	**Description**	**Units**
α	Coefficient for the Q_c and Q_e coefficients in Equation 2.34	[–]
α_B	Baumann factor	[–]
α_c	Volume fraction of phase c	[–]
β	Parameter used to determine r_i in Equation 2.17	[–]
β_d	Surface area density for the dispersed phase d	[$\mathrm{m^{-1}}$]
γ	Ratio of specific heats of the vapour	[–]
Δ	$T_L - T_V$	[K]
Δ_{cap}	$T_r - T_L$	[K]
Δ_{sat}	$T_r - T_{sat}$	[K]

Δ_{sup}	$T_{sat} - T_V$	[K]
λ	$\frac{H_{T\,in} - H_{T\,out}}{(u_b)^2}$	[−]
λ_V	Thermal conductivity of the vapour	[W m^{-1} K^{-1}]
μ	Dynamic viscosity of the vapour	[kg m^{-1} s^{-1}]
ν	Coefficient for the droplet growth law defined in Equation 2.38	[−]
ρ	Density	[kg m^{-3}]
σ	Surface tension	[N m^{-1}]
τ_{flow}	Time constant associated to the the flow expansion	[s]
τ_T	Time constant for a droplet laden flow Equation 2.47	[s]
Φ	Correction term of the equation for NI nucleation rate	[−]
ψ_c	Phase indicator for phase c	[−]
ω	Shaft angular speed	[rad s^{-1}]

Subscripts

Symbol	**Description**
$_*$	Critical quantity
$_0$	Quantity at reference state 0
$_{bulk}$	Droplet bulk quantity
$_{dry}$	Refers to an expansion with dry steam
$_{eq}$	Equivalent quantity

g	Number of molecules in one droplet embryo
in	Inlet quantity
i	Interface between continuum and free-molecular regimes
L	Liquid-phase quantity
out	Outlet quantity
pol	Referred to polytropic or *small-stage* expansion
rev	Quantity after reversion to thermodynamic equilibrium
sat	Saturated steam quantity
ss	Isentropic quantity
$surface$	Droplet surface quantity
s	Static quantity
ts	Total-to-static quantity
tt	Total-to-Total quantity
T	Total quantity
V	vapour-phase quantity

Acronyms

Symbol	**Description**
CFD	Computational Fluid Dynamics

ES	Equilibrium Steam: refers to calculations where the vapour and the droplets are assumed to be in equilibrium
LP	Low Pressure
NES	Non Equilibrium Steam: refers to calculations where no equilibrium is assumed between the vapour and the droplets
PR	Pressure ratio
SCC	Spencer Cannon Cotton
WAM	Curve used to correct for wetness losses

Chapter 1

Introduction

The whole electric energy market, from production plants to end-users, is transitioning towards a sustainable use of raw materials and resources, and a reduction of its carbon foot-print. Renewables provide an increasing share of the total production but, as reported in [1], the fossil plants still meet 64% of the global electricity demand. With the current change in the energy mix, the steam turbines are present in the power generation market with different roles: they are used in fossil, combined cycle, geothermal and concentrated solar plants, but also in waste-to-energy and heat recovery applications. Therefore, they still play a primary role in the energy production market. In this scenario, the improvement of the efficiency of the power plants and the reduction of the waste of energy appear to be instrumental to reach the goal of sustainability and low emission. The current trends in the steam turbine developments and researches, like in the case of low volume flow operation (see Hoznedl et al. [2] and Mambro et al. [3] for example) or reduced start-up time (e.g. Seiler et al. [4], Girezzi et al. [5], and Bucciarelli et al. [6]),

show that steam turbine manufacturers are working actively to improve the performance of their products. The contribution of the LP section to the power delivered by a steam turbine can be as high as 40%, therefore it is no mystery the interest of the industry in developing methodologies to improve the LP stage efficiency. In order to maximize the thermal efficiency of a steam plant, it is very convenient to reduce the condenser pressure as much as possible. In fact, a reduction of 1 kPa at the exhaust flange can be worth 0.5% on the Heat Rate of the plant.

Reducing the exhaust pressure impacts the design of a LP section in different ways. The first one is the increase of the annulus area at the exit of the last stage blade, required by the lower density of the steam. Longer last stage rotating blades support the annulus area increase and enable the change from four-flow to double-flow machines, with obvious benefits in terms of cost reduction. The second kind of impact is that reducing the condenser pressure leads to an increased wetness level at the steam turbine exit, which in turn causes the erosion of the rotating blades and the reduction of the aerodynamic efficiency of the stages. These two issues are as old as the steam turbine itself and were recognized by Baumann in his celebrated paper [7]. In this way, the design of long blades becomes a challenging task, because of the high mechanical stress, of the risk of failure caused by high vibrations, and because of the aggressive three-dimensional design of the stages which is needed to avoid negative root reactions degree and high Mach number regions (for a comprehensive review of the implications see Gyarmathy [8] and Havakechian et al. [9]).

All these constraints are summarized in the Figure 1.1 (adapted from [8]) where the design space for a low-pressure stage made of stainless steel is represented using the exhaust area and the

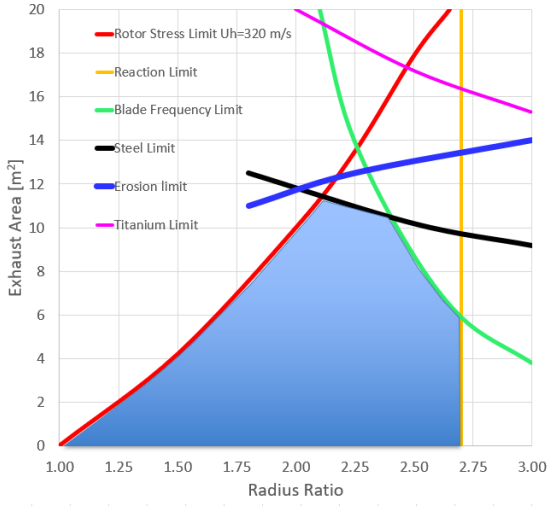

Figure 1.1: Low pressure stage design space

tip-to-hub radius ratio RR.

Reducing the exhaust pressure increases the wetness content of the steam at a level in the range 5% to 18%, depending on the application. As the liquid and the vapour phases of the steam follows different thermodynamic paths during their expansions, and the steam departs from the equilibrium condition, some losses arise, which can be significant as the wetness increases. A well-known rule to quantify these losses is due to Baumann [7], who proposed a simple empirical correlation. The original rule estimates 1% of efficiency drop for 1% of average wetness. Therefore, an easy ballpark assessment is that the impact of moisture losses on the turbine overall performance can be as high as 4%.

The traditional development process for the LP section involves many contributors and requires many steps in order to

meet a long list of requirements for mechanical integrity, aerodynamic performance, manufacturability, layout, and costs. At the end of the development process, because of all the uncertainties and difficulties of the design the companies are forced into an expensive validation step to assess the aeromechanical behaviour and the performance level of the LP section. Testing a sub-component or testing a scaled model of the LP section are the approaches currently used in order to reduce this financial effort (e.g. [10] and [11]). In any case, testing campaigns are run at a limited number of operating conditions.

Traditionally, a system of correlations is used to build a performance model of the LP module. In this way it is possible to expand the usage of a limited set of experimental data to cover the application range encountered in the steam turbine market. Another approach, which has become feasible during the last decade, is the usage of CFD calculations.

As far as the performance is concerned, a large part of the uncertainty is related to the losses caused by the moisture content in the flow. As computational fluid dynamics has evolved, designers have exploited new tools to improve the turbine performance accounting for non-equilibrium effects. However, recent publications (e.g. Starzmann et al. [12]) have shown that a considerable uncertainty in nucleation theory and droplets growth law exist, and no common modelling approach exists as well. For this reason, the accuracy of CFD, for designing and predicting the performance of LP stages is still under a controversial and stimulating debate.

The present PhD Thesis addresses the problem of the performance predictability of the LP stages of the steam turbines. Its final purpose is to provide a methodology to analyse and design the LP stages of the steam turbines thereby reducing the uncer-

tainties arising from the usage of correlations and supporting the reduction of the development cost of new LP stages.

The Thesis is organized as follows:

- In chapter 2 the theoretical foundations for condensing/wet steam analysis are discussed. The correlations used throughout this Thesis are also described.

- In chapter 3 the numerical method used to solve the system of the partial differential equations used to model the fluid-dynamics of the two-phase steam is outlined.

- In chapter 4 the analysis results of two test cases representing two planar nozzles are presented. The accuracy in predicting of the nucleation position and in estimating the nucleating droplet size is also discussed.

- In chapter 5 the analysis results of a test case representing the geometry of a rotor blade tip are reviewed. The accuracy in predicting the losses caused by the nucleation and growth of the water droplets is discussed. The numerical results are compared with some correlations available from literature.

- In chapter 6 the analysis results of a test case representing the geometry of LP 3-stage module are presented, with a major focus on the accuracy of the prediction of overall performance parameters. The numerical results are compared with some correlations available from literature.

- In chapter 7 the results from all the chapters are surveyed and summarized. The criticalities in the use of the correlations together with the improvement in the predictability

achieved using CFD methods are discussed. Future directions for research and improvements to the current work are also suggested.

Chapter 2

THE THEORETICAL FRAMEWORK

In the thermodynamic conditions typical for the low pressure stages of the steam turbines, the water droplets do not nucleate when the saturation temperature and pressure conditions are reached, but after that the steam has obtained a certain degree of supercooling. Then, some energy is released during the nucleation and the equilibrium pressure and temperature are restored, but at the cost of some efficiency reduction. Thereafter, the droplets start to grow following the expanding vapour. In doing so, the steam condensates on their surfaces, releasing a consistent amount of energy in form of latent heat. A temperature difference between the droplet surface and the vapour is established, so that the latent heat energy is transferred back to the vapour causing additional losses. These two aspects in the theory, the homogeneous nucleation and the droplet growth, are the subject of this chapter. The theoretical estimate of the losses caused by the nucleation and growth of droplets are addressed as well.

2.1 PHYSICAL MODELS

2.1.1 THE DROPLET NUCLEATION

The well-known state diagram of the steam is built upon the assumptions that the flow transformations happen in a quasi static manner, and that, at any time, the thermodynamic properties and the velocities are uniform in the considered volume of fluid. As far as a mixture of steam and water is considered, this means that the transformations are slow enough to have thermal and mechanical equilibrium inside the fluid, and that the interphase between the water and the vapour phase (the so-called meniscus) is a planar surface. In fact, in a mixture of droplets and vapour enclosed adiabatically and kept at constant volume, all the droplets evaporate, and the amount of bulk liquid increases correspondingly as the system evolves towards the thermodynamic equilibrium.

Therefore, the widely accepted common statement that cooling the steam below its saturation temperature leads to water formation becomes incorrect in a wide variety of situations where the rate of change of the vapour conditions combines with the absence of foreign materials or wall surfaces which could assist the molecules seeking to condense in a well-behaved manner.

The expansion rate is introduced in Gyarmathy [13] to conveniently describe the rate of change of the vapour conditions. It is defined as $\dot{P} = -\frac{d}{dt} ln(P)$, and it is built using the Lagrangian derivative of the pressure. In the conditions found in the steam turbines, the expansion rate $\dot{P}$ can be as high as $10000 s^{-1}$. In these cases, as the steam reaches the saturation condition, the water phase formation is delayed, and the vapour keeps expanding dry so that a certain degree of supercooling is reached. After that, the formation of water starts at first in the form of tiny

droplets containing 30 to 100 molecules, and then proceeds by growing the droplets up to a final size of $10^{-8}m$ to $10^{-6}m$.

The theoretical framework used to describe the nucleation process includes aspects from both classic [14] and statistical [15] thermodynamics. Following the first reasoning, the nucleation process can be analysed under the assumption of a constant temperature and pressure transformation. Under this assumption, the Second Law of the Thermodynamics states that a certain event can occur spontaneously if the free energy is lowered in the process.

Let's consider a mass m of vapour at a pressure P, and temperature T, with $P > P_{sat}(T)$. The free energy balance for the formation of a droplet of radius r can be written as follows:

$$\Delta G = \Delta G_{surface} + \Delta G_{bulk} \tag{2.1}$$

where first term is simply:

$$\Delta G_{surface} = 4\pi r^2 \sigma \tag{2.2}$$

and the second one is:

$$\Delta G_{bulk} = -\frac{4}{3}\pi r^3 \rho_L R T \ln\left(\frac{P}{P_{sat}}\right) \tag{2.3}$$

The plot in Figure 2.1, adapted from Young et al. [16], shows the Equation 2.1 in non-dimensional form for different values of $\frac{P}{P_{sat}}$ and temperature $T = 100^0 C$. From the plot, it can be seen that an energy barrier makes small droplets impossible to form and grow not only in superheated vapour, but also when a certain value of supersaturation is present. On the other side, large droplets in supersaturated steam are clearly unstable and tend to grow indefinitely. The critical value of the radius can be

easily obtained by looking the maximum in Equation 2.1:

$$r_* = \frac{2\sigma}{\rho_L R T_V \ln(\frac{P}{P_{sat}})} \tag{2.4}$$

The energy barrier to form a droplet of radius r_* is then:

$$\Delta G_* = \frac{4}{3}\pi r_*^2 \sigma = \frac{16\pi\sigma^3}{3[\rho_L R T_V \ln(\frac{P}{P_{sat}})]^2} \tag{2.5}$$

The form of the previous Equation 2.5 and Equation 2.4 is such that increasing the supersaturation of the steam reduces very quickly the energy barrier and the critical size of the droplet. This is shown in Figure 2.2 However, as droplets can only grow molecule by molecules, it would appear clear that nucleation is not possible from a thermodynamic point of view.

Despite the results herein discussed, in a superheated steam does exist a population statistically steady of tiny droplets, called embryos, formed by only few molecules of water. The statistical distribution of these small droplets is expressed using a Boltzmann-like distribution:

$$n_g = n_1 e^{-\Delta G/kT} \tag{2.6}$$

where g is the number of molecules in the embryos, n_g is the number of embryos of size g per unit of volume, n_1 is the total number of molecules in the system per unit volume and can be approximated by the concentration of monomers. Following the reasoning of the statistical thermodynamics, the so-called classical nucleation rate equation J_{class} has been obtained in [15] as:

$$J_{class} = Q_c \frac{n^2}{\rho_L} \sqrt{\frac{2\sigma m}{\pi}} e^{-\Delta G/kT} \tag{2.7}$$

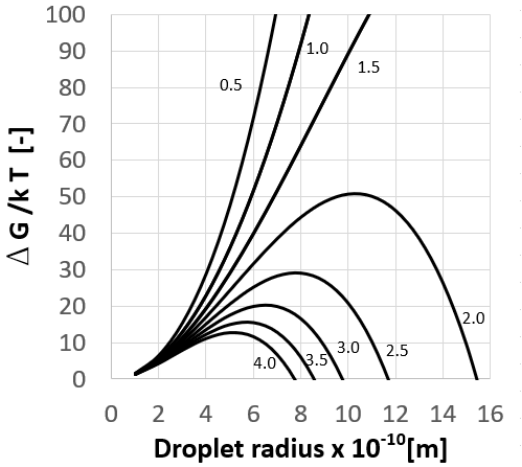

Figure 2.1: Free energy change in the formation of a droplet at 100^0C

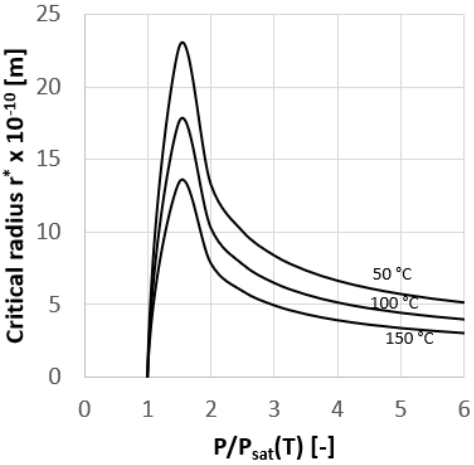

Figure 2.2: Critical radius for different supersaturation conditions and vapour temperatures

Then, making use of the kinetic theory equation $P = nkT$ and of the relation $k = \overline{R}/N_A$ between the Boltzmann constant k, the gas universal constant $\overline{R}$ and the Avogadro number N_A the following equation is obtained which is of more easy use in calculations [16]:

$$J_{class} = Q_c \frac{\rho_V^2}{\rho_L} \sqrt{\frac{2\sigma}{\pi m^3}} e^{-\Delta G/kT} \tag{2.8}$$

The J_{class} has been revised to account for the fact that the growing droplet is heated above the vapour temperature. The resulting correction [17] has the effect of reduce the nucleation rate by a factor 50. The non-isothermal equation for the nucleation rate is:

$$J_{NI} = \frac{1}{1+\Phi} J_{class} \tag{2.9}$$

where

$$\Phi = \frac{2(\gamma - 1)}{\gamma + 1} \left[\frac{L}{RT_V} \left(\frac{L}{RT_V} - \frac{1}{2} \right) \right] \tag{2.10}$$

Over the years, several corrections have been proposed by different researchers to improve the Equation 2.8. For a recent review of the most promising ones the paper [18] should be referred. However, as confirmed recently in [12], there is no common agreement on the equations that should be used for the nucleation. As a matter of fact, throughout this Thesis, Equation 2.9 will be used for all the calculations.

2.1.2 THE DROPLET GROWTH

A second aspect in the wet steam theory concerns the growth of the droplets after the nucleation. As already discussed in the previous subsection 2.1.1, the nucleation of a droplet requires a surplus of energy for the generation of its surface. Broadly speaking, it means that after the nucleation, the number of the droplets stays nearly constant as long as the vapour and the droplets stay in mutual thermal equilibrium.

The droplet growth is analysed with reference to various flow regimes, which are specified by the value of the Knudsen number, Kn, defined as the ratio between the mean free path of a vapour molecule, $\tilde{l}$, to its diameter. Even if just approximated, the traditional division [13] of the Kn range is:

	Kn	< 0.01	: Continuum flow
$0.01 <$	Kn	< 0.2	: Slip flow
$0.2 <$	Kn	< 5	: Transition flow
$5 <$	Kn		: Free molecular flow

Table 2.1: Energy transfer range

When the heat transfer process occurs in the free molecular regime, then $Kn >> 1$ and the methods of kinetic theory can be used. In this case, the energy balance for a droplet can be written [19]:

$$L\frac{dM}{dt} = Mc_L\frac{dT_L}{dt} + 4\pi r^2\frac{P}{\sqrt{2\pi RT_V}}\frac{\gamma+1}{2\gamma}c_p\left(T_L - T_V\right) \quad (2.11)$$

The Equation 2.11 is the balance between the energy released to the droplet in form of latent heat L, the thermal energy stored by the droplet itself and the net energy gained or lost upon the vapour molecules arrival or departure. As the storage term is

negligible with respect to the other terms, the Equation 2.11 can be rewritten as:

$$L\frac{dr}{dt} = \frac{P}{\sqrt{2\pi RT_V}}\frac{\gamma+1}{2\gamma}c_p\left(T_L - T_V\right) \tag{2.12}$$

When the heat transfer process occurs in the continuum regime, then $Kn << 1$ and the more familiar methods can be used. The energy balance can be written:

$$L\frac{dM}{dt} = 4\pi r^2\frac{\lambda_V}{r}\left(T_L - T_V\right) \tag{2.13}$$

which can be rewritten as:

$$L\rho_L\frac{dr}{dt} = \frac{\lambda_V}{r}\left(T_L - T_V\right) = \frac{\lambda_V}{2r}Nu\left(T_L - T_V\right) \tag{2.14}$$

where Nu is defined $Nu = h(2r)/\lambda_V$ and is equal to 2. It is also worth observing that this value is relevant for a sphere in a quiet medium. This is generally acceptable when the droplets are very small and the relative motion between the vapour phase and the droplets is negligible. However, as soon as the droplets grow and their inertial mass is increased, the effects of the relative motion must be included. Therefore, the correction [20] has been introduced in order to account for the effects of the Reynolds and Prandtl numbers. The equation that will be used for Nu is:

$$Nu = 2 + 0.6Re^{1/2}Pr^{1/3} \tag{2.15}$$

The intermediate regime between the free-molecular and the continuum one is further divided in two parts, called slip and transition regimes. The slip flow is characterized by small deviations with respect to the continuum regime, so that the Navier-Stokes equations can be retained but the assumption of wall adhesion of

the molecules is eliminated. Therefore, in this regime, the temperature and the velocity are assumed to be discontinuous at the wall, but it is still possible to set up a theory consistent with the tests. Instead, the transition regime has presented persistent difficulties to a theoretical analysis.

The approach followed in [21] to develop a multirange expression, valid through the full Kn range, is to extrapolate the equations for the continuum regimes and merge it smoothly to the free-molecular one, in analogy to what found for the drag forces. In that way, a simple expression can be obtained:

$$L\rho_L \frac{dr}{dt} = \frac{\lambda_V}{2r} \frac{Nu}{1 + 3.18Kn} (T_L - T_V) \tag{2.16}$$

A more refined approach has been obtained in [22], where the free molecular regime and the continuum regime have been merged, assuming an interface between the free-molecular regime and the continuum regime at a radius r_i, defined as:

$$r_i = (1 + \beta\tilde{l}) \tag{2.17}$$

where the parameter β is used as a tuning parameter, and it is generally assumed equal to 2.

The resulting equation for the droplet growth can be written:

$$L\rho_L \frac{dr}{dt} = \frac{\lambda_V}{2r} \frac{Nu\,(T_L - T_V)}{\frac{1}{1+2\beta Kn} + \frac{\sqrt{8\pi}}{1.5}\left(\frac{2\gamma}{\gamma+1}\right)\frac{Kn}{Pr}} \tag{2.18}$$

For steam, assuming $\gamma = 1.3$, the equation becomes:

$$L\rho_L \frac{dr}{dt} = \frac{\lambda_V}{2r} \frac{Nu\,(T_L - T_V)}{\frac{1}{1+2\beta Kn} + 3.78\frac{Kn}{Pr}} \tag{2.19}$$

The Equation 2.16 and Equation 2.19 can be further simpli-

fied by developing a relation between the various temperatures and pressures relevant for the problem of a growing droplet.

This relation has been developed in [16] and has been obtained as follows. Let's split the difference between the droplet temperature T_L and the temperature T_V of the vapour using $T_{sat}(P)$ and T_r, respectively, the flat film saturation temperature and the saturation temperature of the droplet at the given pressure P. From $\Delta = T_L - T_V$ we get:

$$\Delta = [T_r - T_{sat}] + [T_{sat} - T_V] - [T_r - T_L] = \Delta_{sat} + \Delta_{sup} - \Delta_{cap} \tag{2.20}$$

Each term of Equation 2.20 will be obtained in the following paragraph.

As for Δ_{cap}, let's write the usual Kelvin Helmholtz equation:

$$P_{sat}(r) = P_{sat}(T_L) exp\left(\frac{2\sigma_L}{r\rho_L R T_L}\right) \tag{2.21}$$

in the form

$$\ln\left(\frac{P_{sat}(r)}{P_{sat}}\right) = \frac{2\sigma_L}{r\rho_L R T_L} \tag{2.22}$$

The Clapeyron equation:

$$\frac{dP_{sat}}{dT_{sat}} = \frac{L P_{sat}}{R T_{sat}^2} \tag{2.23}$$

written in the integral form is:

$$\ln\left(\frac{P_{sat}(r)}{P_{sat}}\right) = \frac{L_L}{R T_r T_L}\left(\frac{1}{T_L} - \frac{1}{T_r}\right) = \frac{L_L}{R T_L T_r}(T_r - T_L) \tag{2.24}$$

By combining Equation 2.24 and Equation 2.22 it is then possible to write:

$$[T_r - T_L] \simeq \frac{2\sigma_L T_r}{\rho_L L_L r} \tag{2.25}$$

The correspondent equation for T_V can be obtained in a similar way, by evaluating the density of the liquid phase ρ_{LV} at the temperature of the vapour T_V, so that:

$$[T_{sat} - T_V] \simeq \frac{2\sigma_V T_{sat}}{\rho_{LV} L_V r_*} \tag{2.26}$$

which can be combined to give:

$$\frac{[T_r - T_L]}{[T_{sat} - T_V]} = \frac{\sigma_L}{\sigma_V}\frac{L_V}{L_L}\frac{\rho_{LV}}{\rho_L}\frac{T_r}{T_{sat}}\frac{r_*}{r} \simeq \frac{r_*}{r} \tag{2.27}$$

As for the term Δ_{sat}, two possible approaches can be found in the literature. The first one [13] is obtained by neglecting the difference between the two saturation temperatures. Doing so, we get $[T_r - T_{sat}] \simeq 0$ and the Equation 2.20 is simply reduced to:

$$\Delta = \left[1 - \frac{r_*}{r}\right] \Delta_{sup} \tag{2.28}$$

while the Equation 2.16 becomes:

$$L\rho_L \frac{dr}{dt} = \frac{\lambda_V}{2r}\frac{Nu}{1 + 3.18Kn}\left[1 - \frac{r_*}{r}\right][T_{sat} - T_V] \tag{2.29}$$

The second approach [22] is obtained by using the mass continuity equation for the free-molecular regime written at the interface at radius r_i:

$$\rho_L \frac{dr}{dt} = \frac{2}{2 - Q_c}\left[\frac{Q_c P}{\sqrt{2\pi R T_i}} - \frac{Q_e P_{sat}(r)}{\sqrt{2\pi R T_L}}\right] \tag{2.30}$$

and replacing $\rho_L \frac{dr}{dt}$ with the right-hand side of the Equation 2.12 written at the interface. Then solving for $P_{sat}(r)/P$ it results that:

$$\frac{P_{sat}(r)}{P} = \left[1 - \frac{2 - Q_c}{2Q_c}\frac{\gamma + 1}{2\gamma}\frac{c_p}{L}(T_L - T_i)\right]\frac{Q_e}{Q_c}\sqrt{\frac{T_L}{T_i}} \tag{2.31}$$

By equating Equation 2.12, written for the free-molecular regime valid for the inner region enclosed by the interface at radius r_i, to the Equation 2.19 and using the approximated Clausius-Clapeyron equation in the form:

$$[T_r - T_{sat}] \simeq \frac{RT_{sat}^2}{L} \ln\left[\frac{P_{sat}(r)}{P}\right] \tag{2.32}$$

the final relationship is found:

$$[T_L - T_i] = \frac{3.78Kn/Pr}{\frac{1}{1+2\beta Kn} + 3.78\frac{Kn}{Pr}}[T_L - T_V] \tag{2.33}$$

By assuming a linear equation for the condensation and evaporation coefficients:

$$\frac{Q_c}{Q_e} = 1 + \frac{\alpha(T_L - T_i)}{T_{sat}} \tag{2.34}$$

the final equation for Δ_{sat} is obtained:

$$\Delta_{sat} = \frac{RT_{sat}}{L}\left[\alpha - 0.5 - \frac{2 - Q_c}{2Q_c}\frac{\gamma + 1}{2\gamma}\frac{c_p T_{sat}}{L}\right]\delta\Delta \tag{2.35}$$

where δ is defined as:

$$\delta = \frac{3.78Kn/Pr}{\frac{1}{1+2\beta Kn} + 3.78\frac{Kn}{Pr}} \tag{2.36}$$

Therefore, Equation 2.20 becomes:

$$\Delta = \frac{1}{1 - \nu\delta}\left[1 - \frac{r_*}{r}\right]\Delta_{sup} \tag{2.37}$$

where

$$\nu = \frac{RT_{sat}}{L}\left[\alpha - 0.5 - \frac{2 - Q_c}{2Q_c}\frac{\gamma + 1}{2\gamma}\frac{c_p T_{sat}}{L}\right] \tag{2.38}$$

The final droplet growth law obtained from Equation 2.37 and Equation 2.19 is derived in [16] and shown below:

$$L\rho_L \frac{dr}{dt} = \frac{\lambda_V}{2r} \frac{Nu}{\frac{1}{1+2\beta Kn} + 3.78(1-\nu)\frac{Kn}{Pr}} \left[1 - \frac{r_*}{r}\right] [T_{sat} - T_V] \tag{2.39}$$

It can be seen that both the Equation 2.29 and the Equation 2.39 estimate that droplets grow linearly with the supercooling of the vapour for $r > r_*$ and tend to evaporate when $r < r_*$.

2.2 LOSS MODELS

2.2.1 THE NUCLEATION LOSSES

As already discussed, when the dry steam expands to a pressure below the saturation line no droplets are generated until a certain value of supercooling is achieved (see subsection 2.1.1). Therefore, when supercooled and in a metastable condition the thermodynamic state of the steam can be described by the same equations that apply to the superheated steam. After the nucleation of new droplets, the steam reverts to equilibrium conditions, i.e. to a state of minimum internal energy. The term *nucleation losses* refers to the losses that occur when a dry steam in metastable condition reverts to equilibrium by generating a large number of small water droplets and releasing the latent heat of condensation under adiabatic conditions and no work exchange. The transfer of energy in the form of latent heat and the associated losses can be calculated in terms of entropy increase as explained in Gyarmathy [23]. The amount of wetness generated in the process is simply obtained by equating the internal energy "lost" by the supercooled steam to the energy released in form of

latent heat. When this is done the following relation is obtained:

$$Y_{eq} = \frac{c_p}{L}\left(T_{sat} - T_V\right) \tag{2.40}$$

The initial amount of entropy of the supercooled steam is:

$$s_V^{sup} = s_0 + c_p ln\left(\frac{T_V^{sup}}{T_0}\right) - Rln\left(\frac{P}{P_0}\right) \tag{2.41}$$

The entropy at the end of the reversion is:

$$s_V^{rev} = s_0 + c_p ln\left(\frac{T_{sat}}{T_0}\right) - Rln\left(\frac{P}{P_0}\right) - \frac{L}{T_{sat}}Y_{eq} \tag{2.42}$$

Therefore, the increase of entropy in the system is:

$$\frac{\Delta s}{c_p} = -ln\left(\frac{T_V}{T_{sat}}\right) - \frac{L}{T_{sat}}Y_{eq} \tag{2.43}$$

By combining Equation 2.43 and Equation 2.40, and remembering that $\Delta_{sup} = T_{sat} - T_V$ the final equation (see Gyarmathy [23] is obtained:

$$\frac{\Delta s}{c_p} = -ln\left(1 - \frac{\Delta_{sup}}{T_{sat}}\right) - \frac{\Delta_{sup}}{T_{sat}} \tag{2.44}$$

or equivalently:

$$\frac{\Delta s}{c_p} = -ln\left(1 - \frac{LY_{eq}}{c_p T_{sat}}\right) - \frac{LY_{eq}}{c_p T_{sat}} \tag{2.45}$$

2.2.2 THE THERMODYNAMIC RELAXATION LOSSES

After the nucleation the droplets and the vapour phase are in thermal and mechanical equilibrium. As the expansion proceeds, the steam keeps condensing on the droplets. The latent heat is

released to the droplets, whose temperature starts to increase, while the vapour temperature lags behind its saturation value. The difference in temperature between the two phases causes a transfer of thermal energy so that the equilibrium between them is restored to a certain extent. The losses associated to this energy transfer are called *thermodynamic relaxation losses*. The extent to which the thermal equilibrium is achieved depends on the balance between two different terms:

- the time constant τ_T associated to the transfer of the energy amount needed to restore the thermal equilibrium between the phases
- the time constant τ_{flow} associated to the flow expansion

The amount of supercooling achieved during an expansion can be evaluated if the expansion rate is constant, or piecewise constant. Under this assumption, the following analytical solution is presented in Young [24]:

$$\Delta_{sup}(t) = \Delta_{sup}^{(0)} e^{-t/\tau_T} + \tau_T F \dot{P} \left(1 - e^{-t/\tau_T}\right) \tag{2.46}$$

The parameter F represents the influence coefficient of the expansion rate $\dot{P}$ on the vapour supercooling, and τ_T is the time constant of the system. They are defined respectively by Equation 2.47 and Equation 2.48 below:

$$\tau_T = \frac{(1-Y)c_p\rho_L r^2 \left(1 + 3.78\frac{Kn}{Pr}\right)}{3\lambda_V Y} \tag{2.47}$$

$$F = \frac{P}{(1-Y)c_p\rho_{sat}} \left[\frac{cT_{sat}}{L} - (1-Y)\alpha T_V \frac{\rho_{sat}}{\rho_V}\right] \tag{2.48}$$

When the droplets are very small, then $\tau_T \to 0$, and $\Delta_{sup} \to 0$ as well. In this case the flow evolves in thermodynamic equi-

librium, so that:

$$Y \to Y_{eq} = Y_0 + \frac{(1-Y)c_p}{L} F\dot{P}t \tag{2.49}$$

When the droplets become large the τ_T increases, and the supercooling Δ_{sup} increases as well, eventually up to its limit value equal to:

$$\Delta_{sup} \to \tau_T F\dot{P} \tag{2.50}$$

If this value is high enough, then a second nucleation starts with additional nucleation losses. Otherwise, a nearly constant number of droplets evolve.

Several authors provide analytical methods to estimate the losses caused by the heat transfer between the droplet and the vapour phase. Based on the Equation 2.46, the following equation is derived in Young [24]:

$$\frac{\Delta s}{c_p} = \frac{1-Y}{T_{sat}^2}\left\{ \frac{\Delta_{sup}^{(0)\,2}}{2}\left(1-e^{-2t/\tau_T}\right) + F\dot{P}\tau_T\Delta_{sup}^{(0)}\left(1-e^{-t/\tau_T}\right)^2 + \right.$$
$$\left. + \left(F\dot{P}\tau_T\right)^2\left[\frac{t}{\tau_T} - 2\left(1-e^{-t/\tau_T}\right) + \frac{1}{2}\left(1-e^{-2t/\tau_T}\right)\right]\right\} \tag{2.51}$$

Other formulations exist in the literature. The one in Gyarmathy [21] is:

$$\Delta\eta_{pol} = 0.04\frac{1-Y}{Y}\frac{\rho_L}{\rho_V}\frac{1+4Kn}{\mu PKn^2}\dot{P} \sim \frac{\Delta_{sup}}{T} \tag{2.52}$$

with the usual definition for Kn:

$$Kn = \mu\frac{\sqrt{RT_V}}{rP} \tag{2.53}$$

A similar equation is presented in Kreitmeier et al. [25]:

$$\Delta\eta_{pol} = 0.12\frac{\tau_{th}}{\tau_{flow}} = 0.12\frac{1-Y}{Y}\frac{\rho_L c_p r^2}{3\lambda_V}\left(1+4Kn\right)\dot{P} \tag{2.54}$$

An equation obtained under the assumption of constant supercooling ΔT is present in Starzmann et al. [26], which is derived using:

$$\Delta s = \frac{\dot{q}}{T_V} - \frac{\dot{q}}{T_L} \tag{2.55}$$

By assuming that:

$$\dot{q} = L\Delta Y \tag{2.56}$$

$$T_L \sim T_{sat} \tag{2.57}$$

a simplified version is obtained:

$$\frac{\Delta s}{c_p} = \frac{T_{sat}-T_V}{T_{sat}T_V}\Delta Y\frac{L}{c_p} \tag{2.58}$$

Using the results of the previous chapter, it is possible to write down a modified version of Equation 2.45, where the increase of the wetness caused by the expansion is used instead of Y_{eq}. In doing so, the following equation is obtained:

$$\frac{\Delta s}{c_p} = -ln\left(1-\frac{L\Delta Y}{c_p T_{sat}}\right) - \frac{L\Delta Y}{c_p T_{sat}} \tag{2.59}$$

2.2.3 THE BAUMANN FACTOR

One of the first attempt to quantify the losses caused by the presence of wetness in the low pressure section of the steam turbines is due to Baumann [7]. Based on the data available at that time, he proposed a $1\% - 1\%$ rule, that is a 1% of efficiency drop with respect to the dry expansion for a 1% of average moisture, which means $\alpha_B = 1$ in the equation below:

$$\Delta\eta = \eta_{dry} - \eta = \frac{\alpha_B}{2}\left(Y_{in} + Y_{out}\right) \tag{2.60}$$

The test data collected in the following years show a large variability of the Baumann factor α_B. One of the most referenced set of data, the one in Miller et al. [27] and Spencer et al. [28], shows in Figure 2.3 that the drop in efficiency at low values of wetness is very high, while the trend slowly collapses on the Baumann line as the wetness increases. Using the data available

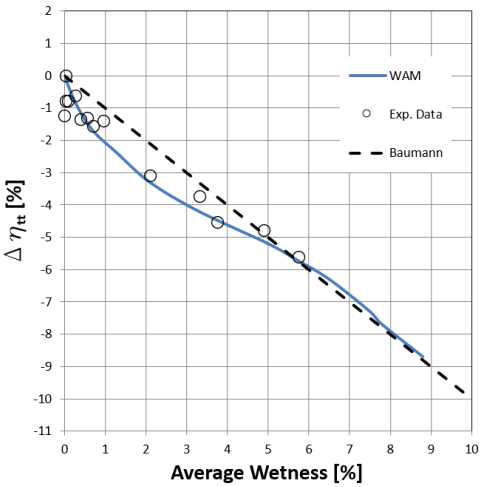

Figure 2.3: Efficiency drop as a function of average wetness

from Spencer et al. [28], it is possible to have a closer look to the losses at different values of average wetness. In order to do this, the experimental data are shown in Figure 2.3 together with the Baumann line. In the same plot, it is shown the polynomial fit of the experimental data (called *WAM*) proposed by Spencer et al. [28]) and used to correct the efficiency of a turbine for the wetness effects. The surprising large drop of the efficiency at low level of wetness becomes comprehensible as soon as it is recognized that the points shown in the plot belong to different expansion lines, and that this difference must be compensated. To do this, the data are elaborated in terms of polytropic efficiency η_{pol} and thermal reheat factor RH as suggested in Gyarmathy [23]. The following definition for RH is used:

$$RH = \frac{\eta_{tt}}{\eta_{pol}} \tag{2.61}$$

After doing so, the Figure 2.4 for the thermal reheat factor and the Figure 2.5 for the polytropic efficiency are obtained. The drop of the polytropic efficiency in Figure 2.5 is fitted using a linear function of the average wetness. Finally, applying the $\Delta\eta_{pol}$ to a dry expansion, the final estimate of the wetness losses is obtained. The wetness losses without the effect of the thermal reheat shown in Figure 2.6, from which it is concluded that the actual effect of the wetness is nearly one half of what generally thought, i.e. $\alpha_B \sim 0.5$.

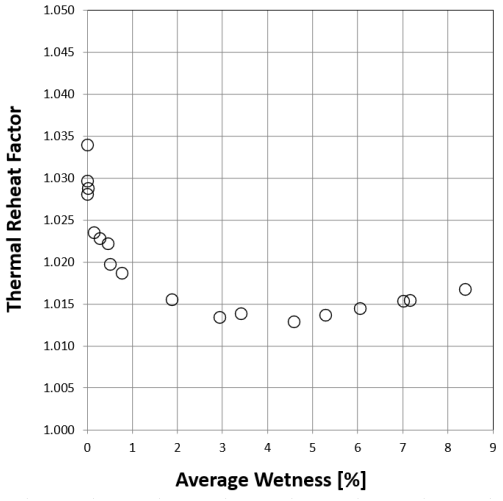

Figure 2.4: Thermal Reheat Factor for the considered test data

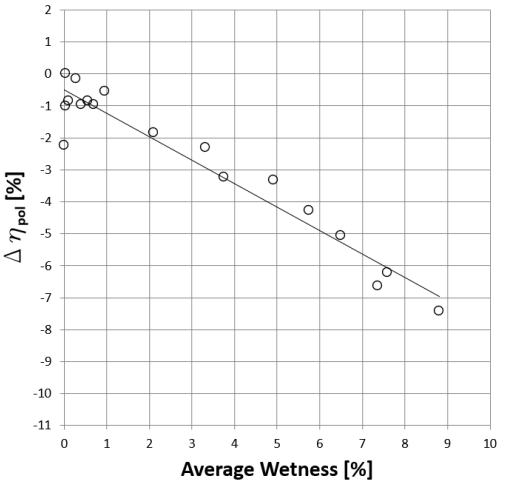

Figure 2.5: Polytropic efficiency drop as a function of average wetness

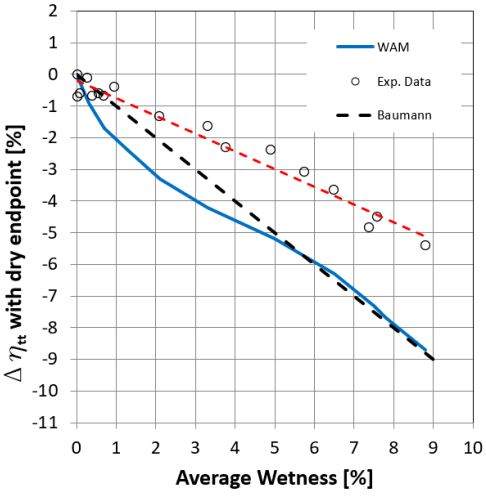

Figure 2.6: Efficiency drop with dry endpoint

2.2.4 THE KINETIC ENERGY LOSSES

An important piece of a LP performance model is the one that estimates the kinetic energy leaving the last stage and entering the exhaust system. As the LP section of a steam turbine is also the last one before the condenser, the kinetic energy at the exit of the last stage rotating blade is an important performance parameter. Even if part of it is recovered in the exhaust system, it is considered a loss, and therefore named leaving losses (LL). Its impact for this kind of LP section ranges between 5 points to 10 points of efficiency. The estimate of this loss changes if the vapour and the droplets are assumed to be in equilibrium or not. In the following discussion, the two cases are labelled equilibrium steam (ES) and non-equilibrium steam (NES) respectively. Gyarmathy [13] explains that the kinetic energy lost at the turbine exit is affected by non-equilibrium effects because

of the inter-phase drag and supercooling of the steam. By assuming that for a given operating condition and rotating velocity the kinetic energy is proportional to the axial component of the steam velocity, it can be stated that:

$$\Delta LL = \frac{k^2}{2}\left[(u_x^2)^{ES} - (u_x^2)^{NES}\right] = \frac{k^2}{2}(u_x^2)^{ES}\left[1 - \frac{(\rho^2)^{ES}}{(\rho^2)^{NES}}\right] \tag{2.62}$$

where it is assumed that the mass flow is fixed so that

$$\dot{m} = (u_x)^{NES} A_{exhaust} (\rho)^{NES} = (u_x)^{ES} A_{exhaust} (\rho)^{ES}$$

By referring to an auxiliary reference state with equilibrium steam at final entropy and pressure using the label $\hat{()}^{NES}$, the density difference between the NES and the ES calculations can be split in two pieces. The first one is due to the fact that the wetness losses move the end point of the expansion line to a state with higher entropy but same pressure. Therefore, they tend to reduce the density of the steam and increase the kinetic energy at the exit of the LP section. Remembering the definition of density of a mixture of steam and water:

$$\frac{1}{\rho} = (1 - Y)\frac{1}{\rho_V} + Y\frac{1}{\rho_L} \tag{2.63}$$

the first piece is

$$\frac{(\rho)^{ES}}{(\hat{\rho})^{NES}} = \frac{1 - (\hat{Y})^{NES}}{1 - (Y)^{ES}} \tag{2.64}$$

The second effect is due to the supercooling present in the NES calculation, and tend to increase the density and reduce the kinetic energy. Its effect in terms of density can be written as:

$$\frac{(\hat{\rho})^{NES}}{(\rho)^{NES}} = 1 - \left(\frac{1}{T_{sat}} - \frac{c_p}{L}\right)\Delta T \tag{2.65}$$

Combining Equation 2.64 and Equation 2.65, and neglecting small terms of higher order, the final correction for the kinetic energy is written as:

$$\Delta LL = LL \left[2 \left(\frac{1}{T_{sat}} - \frac{c_p}{L} \right) \Delta T - 2 \frac{(Y)^{ES} - (\hat{Y})^{NES}}{1 - (Y)^{ES}} \right] \quad (2.66)$$

A correlation widely used to correct the kinetic energy for non-equilibrium effects is the one reported in Spencer et al. [29], labelled *SCC* from the names of the authors of the paper. The equation is repeated here below:

$$\Delta LL_{SCC} = \left[1 - (1 - Y_{out})(1 - 0.65 Y_{out}) \right] LL \quad (2.67)$$

The company to which the author is affiliated has another correlation, labelled as *Legacy*:

$$\Delta LL_{legacy} = 0.19(Y_{out} - 0.01561) \left(\frac{u_b}{350} \right)^2 LL \quad (2.68)$$

where u_b is the blade peripheral velocity.

Chapter 3

THE NUMERICAL METHODOLOGY

In this chapter, the two-phase flow problem is discussed in the context of the nucleating/condensing steam in the low pressure stages of the steam turbines. The differential equations in Eulerian form are introduced showing their relationship with the conventional Reynolds Averaged Navier Stokes equations (RANS). Finally, the equations that describe the nucleation and the growth of the water droplets are shown in the context of the two-phase differential equations that are used for the analyses throughout the present research.

3.1 THE TWO-PHASE FLOW EQUATIONS

3.1.1 AN INTRODUCTION

After the development of the theoretical framework described in the previous sections chapter 2, and its deployment in the industry in the '70s with Gyarmathy [13], the study of the two-phase flow in the low-pressure stages of the steam turbines remained for a long time fundamentally based on the experience built on the numerous tests done on plane nozzles, and on low-order calculation methods. This is because of the inherent difficulties of the two-phase differential equations, but also because of the large computational resources required for their solution.

Generally speaking, a two-phase problem requires two systems of Reynolds Averaged Navier-Stokes equations together with the equations used to predict the turbulence evolution and its effects on the ensemble-averaged flow. More specifically, it could be said that the core of the two-phase problem lies in the set of equations that model the interaction between the two phases. The interface shape and behaviour depend on a large variety of factors, and so do the types of the interaction between the phases. As of today, no general formulation of the two-phase problem exists, and specific model equations are used to solve different problems (see for example, Mamoru et al. [30]).

In some cases, a two-phase flow can be effectively solved by applying each set of equations in its corresponding part of the computational domain, with some additional equations to account for the interaction between the two-phases.
This is generally possible whenever the boundary between the two phases is known and continuous in space and time, like, for

example, when air and water smoothly flow separated inside a horizontal pipe.

In the case of a steam flow with nucleating or growing droplets, one of the phases (i.e. the water) is finely dispersed in the vapour in the form of tiny droplets. This makes the problem to know where each phase is, and the location of the separation interphase between them virtually ill-posed.

However, several assumptions can be done to simplify the problem. The discussion in the previous chapter 2, for example, shows that the analysis can be simplified if the droplets are assumed to be spherical. This is, in general, acceptable, at least as long as they remain small. Under this condition, in fact, the surface tension is greater than the inertial forces and is therefore able to stabilize the interphase surface. A widely accepted rule of thumb for the stability of the surface of the droplets is expressed in terms of the $Weber$ number, which represents the ratio of surface and inertial forces in non-dimensional terms. According to Hinze [31], the limit for the spherical droplet existence is:

$$We = \frac{\rho_V \left(u_{slip}\right)^2 2r}{\sigma} < 5 \tag{3.1}$$

where u_{slip} is the slip velocity between the droplets and the vapour, i.e. $u_{islip} = u_{iV} - u_{iL}$. This limit can be translated in terms of droplet size for different conditions: as an example, for a droplet at a pressure of 1 bar and temperature of $100°C$, a slip velocity $u_{slip} = 10m/s$ means a threshold equal to $r < 0.02$ mm, which is high enough to ensure that the droplets that will be considered in this research are spherical. Such a condition doesn't hold for very large droplets, or for those that detach from the walls and are entrained in the main flow. In both these cases, the u_{slip} gets very large, because of the lag of the droplets

with respect to the main flow, which is caused by their inertia, or because of the way they get exposed to the main flow.
Among the assumptions used to simplify the two-phase problem, one of the most relevant is to give up modelling the deposition of the droplets to the solid walls, which is caused by the turbulent diffusion of the droplets towards the inner part of the wall boundary layer and by the inertia of the droplets that deviate from the main flow direction. The consequence of this assumption, together with the one to renounce to model the coalescence and break-up of the droplets, is that the number of the droplets is constant unless a nucleation occurs somewhere in the domain. This has, in general, little consequences on the accuracy of a performance analysis, because of the large number of droplets nucleating in a steam flow compared to the one depositing on the walls, but it is very relevant if the erosion caused to the rotating blades by the impacting droplets is a concern. Other simplifications are obtained by assuming that the pressures of the phases are equal, the so-called *frozen pressure* assumption. It is important to observe that this simplification doesn't extend to all the aspects that this pressure difference implies. For example, the corrections discussed in the previous subsection 2.1.2 aim to incorporate in the heat transfer between the phases the effects of the fact that the pressure inside the droplets is different from the saturation value and from to the one of the vapour phase. At the same time, the frozen pressure assumption has relevant consequences for the determination of the stagnation pressure, as it enforces a no-exchange interphase condition when the flow comes to rest (see for example White et al. [32]).

The research presented in Yeoh et al. [33] is one of the first attempt to solve the two-phase flow present in the low-pressure stages of a steam turbine. In that case, a streamline curvature

solver is used in conjunction with a set of non-equilibrium wet steam routines. Bakhtar et al. [34] shows the results obtained using a 2D time-marching code to solve the inviscid flow equations for the vapour with the extra terms to account for the droplet nucleation and growth. That code accounts also for the heat transferred from the droplets back into the main flow, with no interphase slip. A later publication, White et al. [35], reports the development of a 2D time-marching unsteady code for condensing steam and the results obtained in plane nozzle analyses. The code architecture is specifically Eulerian for the vapour and Lagrangian for the droplets, and the code is essentially inviscid. In Liberson et al. [36] a 3D implicit solver is developed for inviscid and non-conductive vapour, with additional terms to account for droplets nucleation, and it is used to study the condensing steam in a turbine stage.

Despite the success obtained in predicting the pressure distribution and the droplet size for condensing steam, all these methods do not allow to estimate accurately the effect of the wetness in the complex three dimensional flow typical of the steam turbine applications. The methodology that is used in the present research is described in Gerber et al. [37] and devised by its authors in order to overcome the limits of the Eulerian-Lagrangian approaches, and especially those related to the scaling to large three dimensional problems of transient analyses.

3.1.2 THE CFD EQUATIONS

The differential equations for the solution of the two-phase flow problem in Eulerian form can be obtained from the standard ones by defining for each phase c a phase indicator $\psi_c(x_i, t)$ such that $\psi_c(x_i, t) = 1$ if phase c is present in x_i at time t within Δt and $\psi_k(x_i, t) = 0$ otherwise. In doing so, the volume fraction α_c is therefore defined as:

$$\alpha_c = \frac{1}{\Delta t} \int_{t-\Delta t/2}^{t+\Delta t/2} \psi_c(x_i, t)\, \mathrm{d}t \tag{3.2}$$

so that, in the following discussion, a generic thermodynamic and aerodynamic variable Θ is to be considered phase-c averaged as defined below:

$$\hat{\Theta}_c = \frac{1}{\alpha_c} \frac{1}{\Delta t} \int_{t-\Delta t/2}^{t+\Delta t/2} \psi_c(x_i, t)\Theta\, \mathrm{d}t \tag{3.3}$$

The axiom of continuity Equation 3.4 can be expressed as:

$$\sum_{c=1}^{n_d+1} \alpha_c = \sum_{d=1}^{n_d} \alpha_d + \alpha_V = 1 \tag{3.4}$$

From the definition of α_d, the number of droplets per unit volume can be estimated as:

$$N_d = \frac{\alpha_d}{\frac{4}{3}\pi r_d^3} \tag{3.5}$$

The resulting differential equations for the two-phase problem being considered throughout this research are shown in Table 3.1.

It must be observed that in the present research a source-

specific approach is used, which means that a dispersed phase is defined for each domain included in the analysis. For this reason, the equations for the dispersed phase in Table 3.1 have the index d, meaning that similar equations hold for different dispersed phases.

As for the mass and momentum equations in Table 3.1, they are similar to the standard ones, except for the source terms $S_{V\phi 2}$ and $S_{d\phi 2}$.

In particular, the source term $S_{d\phi 2}$ of the mass-conservation equation contains the term J_d which is defined as in Equation 2.9.

The term $\dot{m}_d$ in the equations refer to the mass transfer for unit volume associated with the heat flow balance of Equation 2.14, so that:

$$\dot{m}_d = \frac{\dot{q}_c + \dot{q}_c}{H_c - H_d} \tag{3.6}$$

where

$$\dot{q}_c = \frac{\lambda_V}{2r_d} Nu_V \left(T_r - T_V\right) \tag{3.7}$$

and

$$\dot{q}_d = \frac{\lambda_L}{2r_d} Nu_d \left(T_r - T_L\right) \tag{3.8}$$

The Equation 3.7 is the equivalent to Equation 2.14, where Nu can have different formulations as in Equation 2.29 or in Equation 2.39. Depending on the size of the droplets, the temperature difference between the droplet inner part and the surface can be considered or neglected. In the first case, $Nu_d = 6$ is assumed in Equation 3.8, while in the second one the Equation 3.8 is replaced by $\dot{q}_d = 0$.

The energy conservation equation is written using two different approaches for the dispersed phases to be consistent with the approach used for Equation 3.8. The first approach, labelled *Energy*(1), is the equation to be used with large droplets. This

equation solves for the specific enthalpy of the droplets, accounting for the heat transfer between the surface and the inner part of the droplets. In the second approach, which is the one adopted in the present research, the equation $Energy(2)$ is used, which is equivalent to the Equation 2.28.

The term β_d in the conservation equations is the surface area density, that is the total surface area of the droplets per unit volume. Its expression, which can be obtained from its definition, is:

$$\beta_d = \frac{3\alpha_d}{r_d} \tag{3.9}$$

Finally, the interphase drag forces are accounted for by using the drag coefficient C_D from the Schiller-Naumann equation (see Schiller et. al. [38]):

$$C_D = max[\frac{24}{Re}(1 + 0.15Re^{0.687}), 0.44] \tag{3.10}$$

Continuum phase	$\frac{\partial(\rho\alpha\phi)_V}{\partial t} + \frac{\partial(\rho\alpha u_j\phi)_V}{\partial x_j} = S_{V\phi 1} + S_{V\phi 2}$		
	ϕ	$S_{V\phi 1}$	$S_{V\phi 2}$
Mass	1	0	$-\sum_{d=1}^{n_d} S_{d\phi 2}$
Momentum	u_i	$-\alpha_V \frac{\partial P}{\partial x_i} + \frac{\partial \alpha_V \tau_{ijV}}{\partial x_j}$	$-\sum_{d=1}^{n_d} S_{d\phi 2}$
Energy	H_T	$-\alpha_V \frac{\partial P}{\partial t} + \frac{\partial \alpha_V Q_{jV}}{\partial x_j} + S_V$	$-\sum_{d=1}^{n_d} S_{d\phi 2}$
Dispersed phase	$\frac{\partial(\rho\alpha\phi)_d}{\partial t} + \frac{\partial(\rho\alpha u_j\phi)_d}{\partial x_j} = S_{d\phi 1} + S_{d\phi 2}$		
	ϕ	$S_{d\phi 1}$	$S_{d\phi 2}$
Mass	1	0	$\dot{m}_d + M_* \alpha_V J_d$
Momentum	u_i	$-\alpha_d \frac{\partial P}{\partial x_i} + \frac{\partial \alpha_d \tau_{ijd}}{\partial x_j}$	$\dot{m}_d u_{id}^U - C_D/8 \beta_d \rho_V \lvert u_{id} - u_{iV} \rvert (u_{id} - u_{iV})$
Energy (1)	H_T	$-\alpha_d \frac{\partial P}{\partial t} + \frac{\partial \alpha_d Q_{jd}}{\partial x_j} + S_d$	$\dot{m}_d H_T^U + \beta_d \dot{q}_d$
Energy (2)	$T_d = T_{sat}(P) - \frac{r_*}{r_d}[T_{sat}(P) - T_V]$ for $2r_d < 1\mu m$		
Number	N/α	0	$\alpha_V \rho_d J_d$
Mixture conservation	$\frac{\partial(\rho\phi)}{\partial t} + \frac{\partial(\rho u_j\phi)}{\partial x_j} = \frac{\partial}{\partial x_j}\left(\Gamma_{eff}\frac{\partial\phi}{\partial x_j}\right) + S$		
	ϕ	Γ	S
Mass (pressure)	1	0	0
Turbulent kinetic energy	κ	μ_t/Pr_k	$\kappa - \omega$ model with scalable wall functions
Specific dissipation rate	ω	μ_t/Pr_ω	

Table 3.1: Governing equations

Chapter 4

PLANE NOZZLE ANALYSIS

In this chapter, a set of user defined functions has been coded to be used in conjunction with the commercial code ANSYS CFX v 18.0 widely used in the turbomachinery community. The results obtained using different modelling hypothesis and parameters have been compared with the experimental data of Moses et al. [39] and with the ones of Binnie et al. [40]. The results of the numerical calculations show that a significant improvement of the accuracy of the performance prediction can be obtained by using the growth law for the droplets developed by Young [22] and that no significant correction is required for the considered cases.

4.1 ANALYSIS OF PLANE NOZZLES

4.1.1 THE MOSES AND STEIN PLANE NOZZLE

The first case examined is the test 203 described by Moses et al. [39]. This test case is one of the most used, because in addition to the static pressure measurements, the authors provided the measurements of the light scattered by the droplets nucleated in the nozzle; the measurements were then elaborated by Young [22] who deduced from those data also the distribution of the droplet radius. This case is suitable for low pressure applications, given the fact that it shows the condensation region at a pressure around $12kPa$. The geometry of the nozzle is shown in Figure 4.1. In order to proceed with the analysis, a computational mesh has been built using ANSYS WorkBench v.18. The computational domain is divided in three parts. A hybrid 3D tetra-mesh has been used in the inlet region of the nozzle, while the remaining part of the mesh is hexahedral. The nucleation region has been refined, as shown in Figure 4.2, in

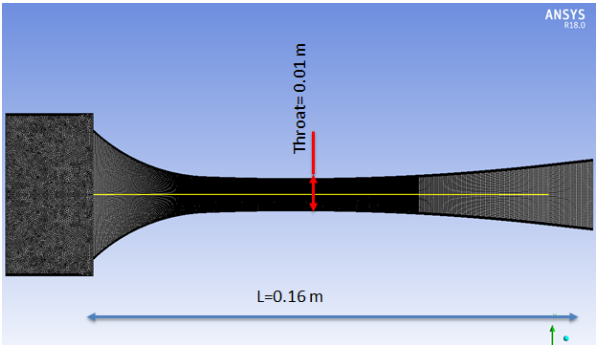

Figure 4.1: The geometry of the Moses and Stein plane nozzle

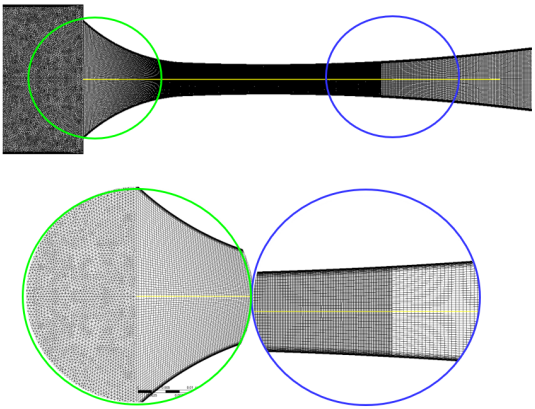

Figure 4.2: The computational mesh of the Moses and Stein plane nozzle

order to have an axial spacing equal to 0.1 mm. The mesh size is 2.3 million of nodes. Wall spacing is chosen in order to have $Y^+ < 1$. The first series of calculations is done using the equation of droplet growth Equation 2.29, which is actually the default formulation used by the code. The results obtained using the Equation 2.9 and the Equation 2.29 are shown in Figure 4.3, where the non-dimensional pressure distribution and the axial position are reported on the vertical and horizontal axis respectively. The nucleation onset can be found in the plot by looking for the pressure bump in the distribution. This pressure bump, often called "condensation shock", is just caused by the deceleration caused by the latent heat energy released by the condensing water. As shown in Figure 4.3, it is possible to match the experimental distribution with a good accuracy using the Equation 2.9 and the Equation 2.29. It is also possible to improve the agreement by modifying the tension surface coefficient of the

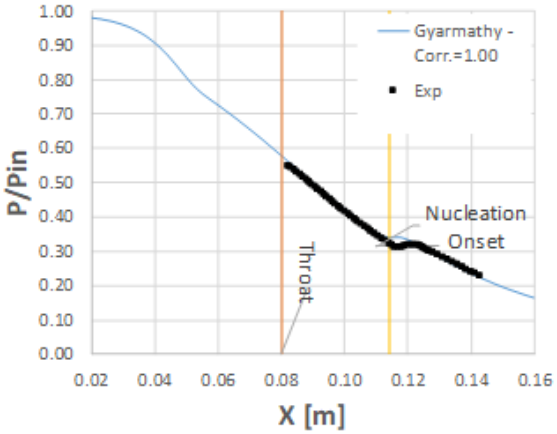

Figure 4.3: The pressure distribution for the Moses and Stein plane nozzle

droplet water. The correction needed, i.e. a multiplier of the tension surface coefficient, is generally small, as the tension surface σ has a crucial impact on the nucleation as shown also in Equation 2.5. An enlarged view of the non-dimensional pressure distribution is shown in Figure 4.4, similar to the previous plot; in this case, however, additional results obtained with different values of the correction for σ are included. It can be seen that, as expected, by increasing the surface tension coefficient it is possible to move downstream the nucleation onset, and that for the case under investigation, a correction equal to 33% is enough to match the position of the nucleation start. The results discussed so far are encouraging. However, as pointed by Young [22] and repeated more recently by Starzmann et al. [12], it is important to match both the pressure and the droplet size distributions in order to have a solid validation of a non-equilibrium steam model. As for our case, the comparison between the numerical

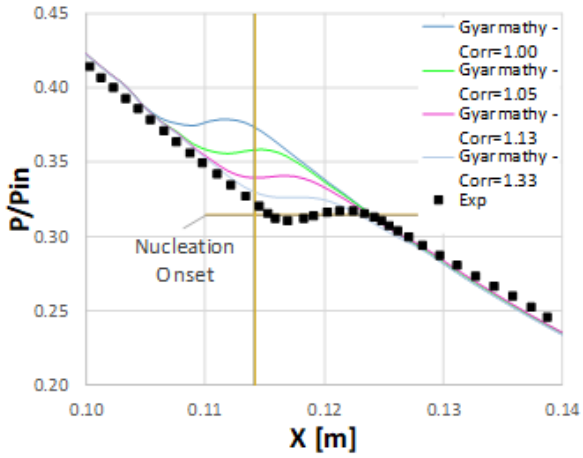

Figure 4.4: Detail of the Pressure ratio distribution for the Moses and Stein plane nozzle

results and the experimental data shows in Figure 4.5 that the droplet growth law in Equation 2.29 is not able to match the experimental data. In order to improve the matching with the experimental data, the Equation 2.39 has been implemented as user defined expression in the CFX code. The improvement in the predictability achieved in this way is shown in Figure 4.6. It is also interesting to observe how the droplet growth affects the pressure distribution. This can be seen in Figure 4.7, where the non-dimensional pressure distributions for the two growth laws without any correction for σ are compared with the experimental data. The interaction between the pressure distribution and the growth law is such that in the present case the Equation 2.39 acts in the same way as the 33% σ correction seen in Figure 4.4 in the delay of the nucleation onset.

This effect of quenching of the nucleation J_{NI} (see Equation 2.9), due to the fast droplet growth expressed in the Equa-

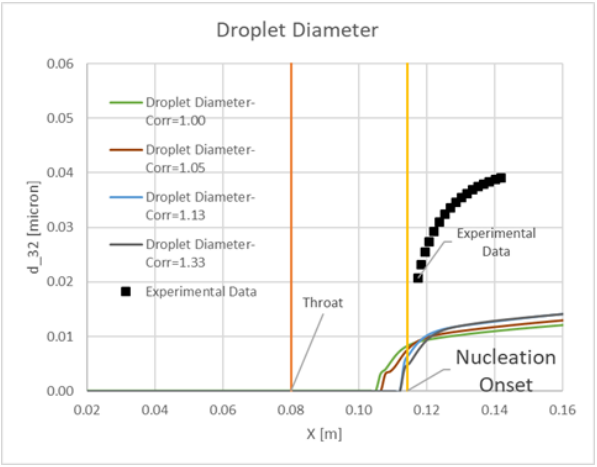

Figure 4.5: Droplet diameter distribution for the Moses and Stein case: Equation 2.29

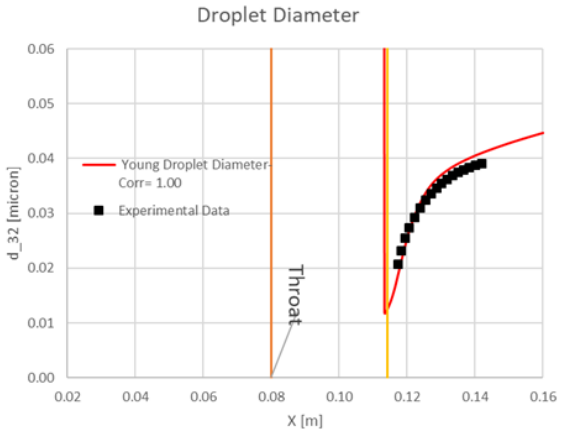

Figure 4.6: The droplet diameter distribution for the Moses and Stein case: Equation 2.39

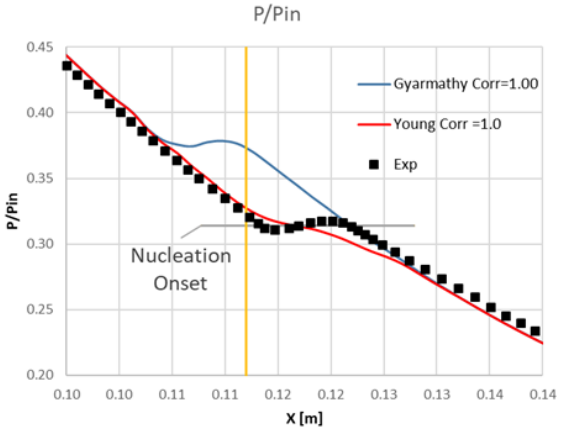

Figure 4.7: The pressure distribution for the Moses and Stein case: Equation 2.29 and Equation 2.39 results

tion 2.39, which in turn results in a rapid reduction of the supercooling, with fewer but larger droplets, is seen also in Figure 4.8, where the values of the nucleation rates obtained with Equation 2.29 and with Equation 2.39 are reported at different axial positions with different correction coefficients of σ. The map of the supercooling of the vapour in Figure 4.9 shows clearly that the supercooling reaches its maximum at $32K$ and drops below $5K$ after the nucleation.

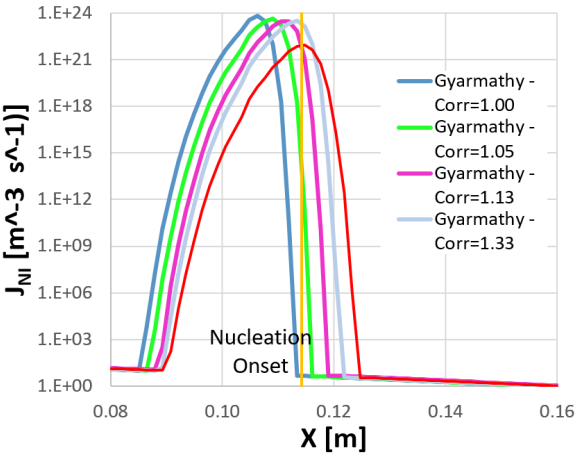

Figure 4.8: The nucleation rate J_{NI} for the Moses and Stein plane nozzle

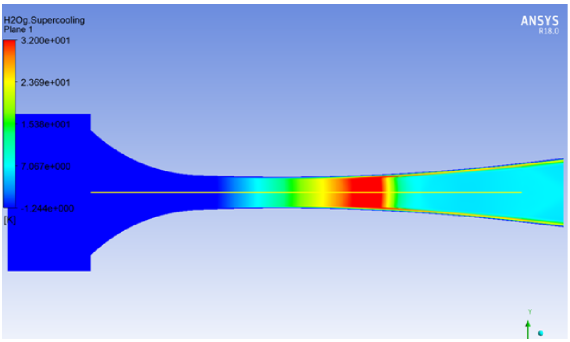

Figure 4.9: The supercooling for the Moses and Stein plane nozzle

4.1.2 THE BINNIE AND GREEN PLANE NOZZLE

The second case examined is the test 96 described by Binnie et al. [40]. This test case is built with a throat larger than in the Moses and Stein case, and with similar expansion rate $\dot{P}$ as high as $10000s^{-1}$. The different size, and the fact that the nozzle is built with cylindrical arcs which blend with a straight section, generates a region where rapid expansion are present, clearly seen in the waves present in the pressure distribution. The geometry of the nozzle is shown in Figure 4.10. In order to proceed with the analysis, a computational mesh has been built using ANSYS WorkBench v.18. The computational domain is divided in three parts. A hybrid 3D tetra-mesh has been used in the inlet region of the nozzle, while the remaining part of the mesh is hexahedral. The nucleation region has been refined, as shown in Figure 4.11, in order to have an axial spacing equal to 0.1 mm. The mesh size is 2.3 million of nodes. Wall spacing is chosen to have $Y^+ < 1$. This case has been analysed using the Gyarmathy Equation 2.29 and the Young Equation 2.39 equations to model the droplet growth.

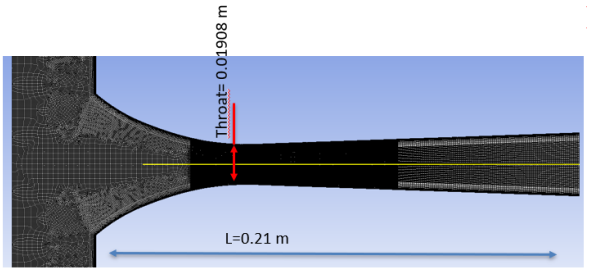

Figure 4.10: The geometry of the Binnie and Green plane nozzle

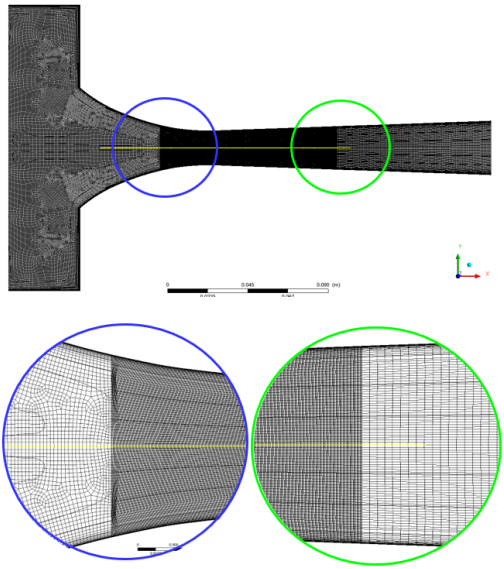

Figure 4.11: The computational mesh of the Binnie and Green plane nozzle

$\mathbf{P_T^{in}}$ $[Pa]$	$\mathbf{T_T^{in}}$ $[K]$	$\mathbf{P_s^{out}}$ $[Pa]$
66189	381.15	27799

Table 4.1: Boundary conditions for test 96

The average values used for the boundary conditions of the test 96 are shown in Table 4.1.

As for the previous case, the Gyarmathy Equation 2.29 model has been used with different values of correction. It can be seen from Fig. 9 that Young Equation 2.39 gives better agreement than Gyarmathy Equation 2.29, even if the mismatch with experimental data upstream of the throat is significant. This is in line with results published by others (see Starzmann et al. [41], for example). It can be seen in Figure 4.13 how the distribution of the wall pressure is perturbed by the expansion waves originated downstream of the throat and being reflected on and on at the wall. These expansion waves are the cause of the wavy pressure distribution in Figure 4.12.

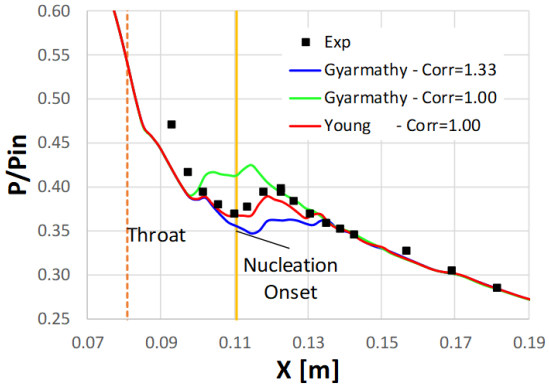

Figure 4.12: The pressure distribution of the Binnie and Green plane nozzle

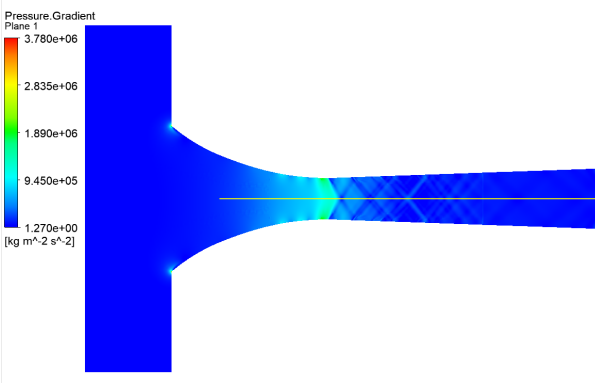

Figure 4.13: The pressure gradient of the Binnie and Green plane nozzle

Chapter 5

CASCADE ANALYSIS

In this chapter, the results of the research done on the plane nozzles are used to study the Bakhtar test cases ([42], [43] and [44]), relevant for cascade configurations. In order to do so, the formulation developed by Young [22] is used, and the effects of different correction levels are investigated. The results have been compared with experimental data available for different pressure ratios, different levels of supercooling and wetness at the inlet. The results have been also elaborated and compared with correlations used in the industry to provide a tangible assessment in terms of predictability improvement.

5.1 THE BAKHTAR CASCADE

The two configurations discussed in the previous chapter 4 allow to test a CFD code at very high expansion number, i.e. high Mach number. However, the nucleation occurs typically at lower Mach number inside the LP sections. From this point of view, the case provided by Bakhtar et al. [42] is a relevant one, as it allows to make tests in a wide range of conditions. The 3D block-structured meshes used for this analysis has been built using the code Numeca $AUTOGRID^{tm}$. The blocking of the mesh is shown in Figure 5.1.

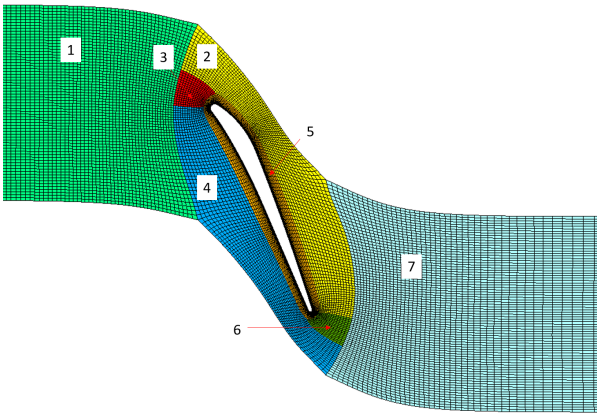

Figure 5.1: Mesh blocking

Four meshes have been used for a sensibility study: the coarsest one has 0.8 million of nodes, while the finest has 12 million of nodes. The differences in terms of efficiency are small at the level of refinement used in this study, as shown in Figure 5.2. Therefore, the mesh used through this study, unless specified, is the one with 1.6 million of cells. This mesh is shown in Figure 5.3

with the relevant dimensions. The traverse plane and the outlet plane are located 5 mm and 150 mm downstream of the blade, respectively, which are equivalent to 0.36 axial chords and 7.8 chords. The wall spacing is chosen to have Y^+ below 10.

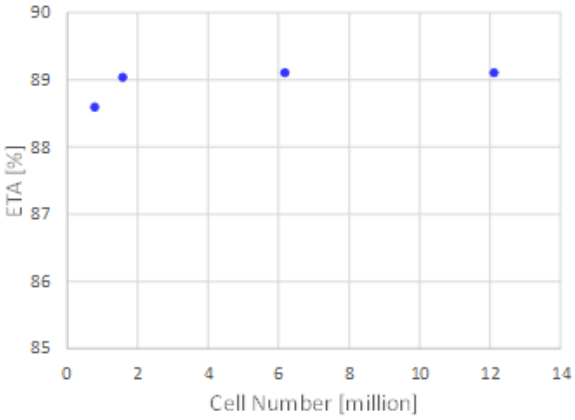

Figure 5.2: Grid sensitivity study (TP27, 1C14SEP9)

5.1.1 THE CASES WITH NUCLEATING STEAM

A first set of cases with nucleating steam has been obtained from Bakhtar et al. [42] and Bakhtar et al. [43] for the pressure measurements on the blade wall and efficiency parameters respectively. The traverse plane position used to evaluate the blade efficiency is shown in Figure 5.3. From the first set, two conditions at pressure ratio equal to 2.33 have been selected:

- the first one is the TP30, with high temperature at the inlet and dry steam at exit
- the second one is the TP27, with inlet steam with $12K$ of supercooling and 5% of moisture at the exit

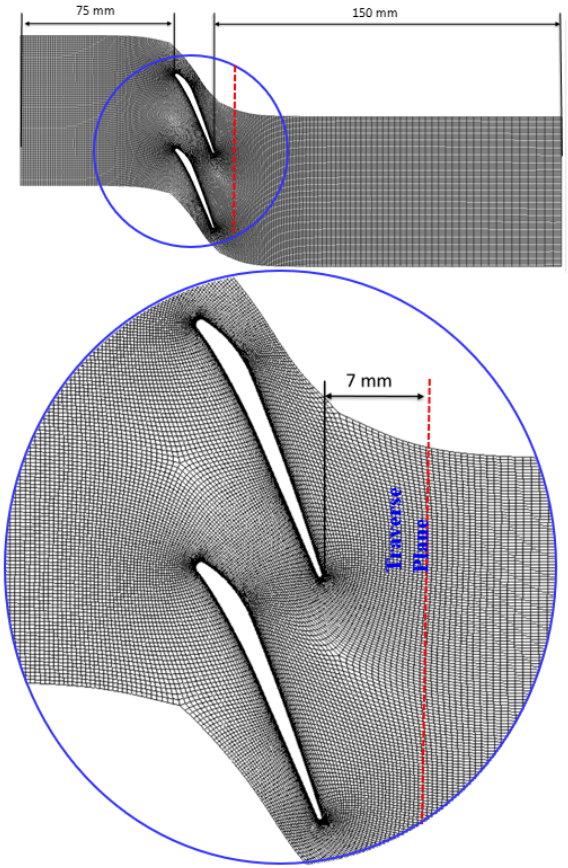

Figure 5.3: The details of the mesh used for the analysis of the Bakhtar cascade.

The two cases have been calculated with the same settings already discussed and with Young Equation 2.39 for the droplet growth. The comparison between numerical results and experiments is shown in Figure 5.4 and Figure 5.5 in terms of non-dimensional pressure on blade wall. The agreement between

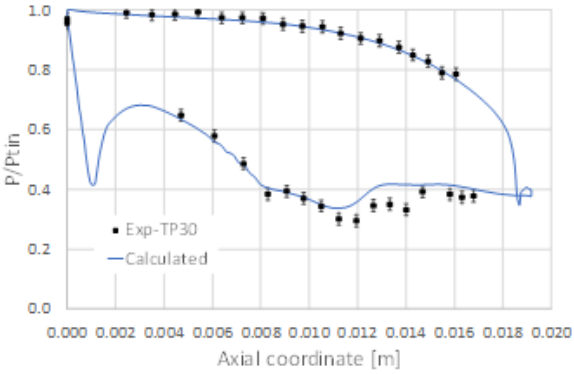

Figure 5.4: Superheated test: Surface Pressure (TP30, 4H15SEP9).

calculated and experimental pressure is generally satisfactory. However, both the previous plots show an evident mismatch in terms of trailing edge pressure, which is possibly due to lack of periodicity in the tests.

Some tests have been done on the correction factor for the surface tension of the water droplets, as suggested in Kermani et al. [45]. The results show that in this case, the matching between calculated values and experiments can be improved by a correction factor equal to 20%, as shown in Figure 5.6. As can be seen from the plot, by increasing the surface tension it is possible to delay the nucleation and move it to a region with higher Mach number. When the correction factor is below 1.2, the condensation starts very close to the leading edge: this is

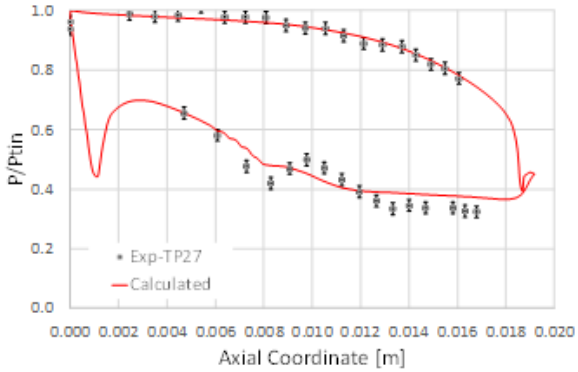

Figure 5.5: Nucleating test: Surface Pressure (TP27, 1C14SEP9).

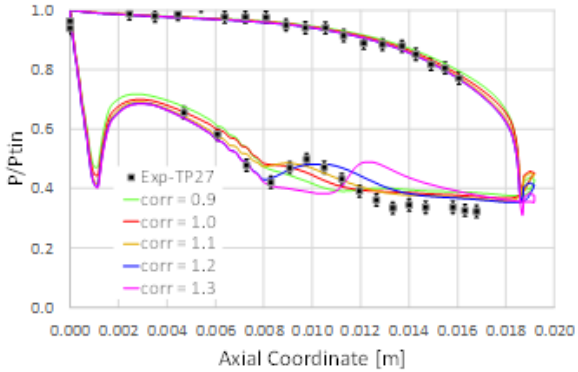

Figure 5.6: Effects of the surface tension (TP27, 1C14SEP9).

evident also because of the different slope of the surface pressure distribution in the region between the leading edge and the axial position $0.008m$. Such a difference is caused by the heat released by the condensing steam and disappears as soon as the nucleation front is moved downstream.

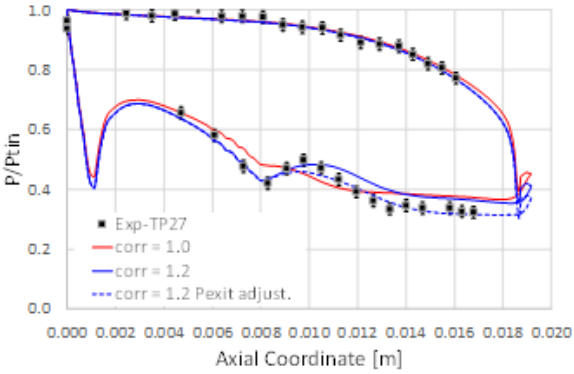

Figure 5.7: Adjustment of the exit pressure (TP27, 1C14SEP9).

Adjusting a little bit the exit pressure helps to improve the matching with the experimental data, as shown in Figure 5.7.

As the front moves downstream, the intensity of the nucleation is increased thereby causing the so-called condensation shock on the blade suction side.

Additional improvement in the matching has been obtained by refining the mesh to a 6.2 million of nodes (see Figure 5.8). It is also interesting to observe that moving the nucleation downstream has a significant effect in terms of bladerow efficiency, as shown in Figure 5.9.

In order to assess the predictive capability of the CFD methodology, the set of data from Bakhtar [43] has been analysed. The set includes data of bladerow efficiency for pressure ratio in the

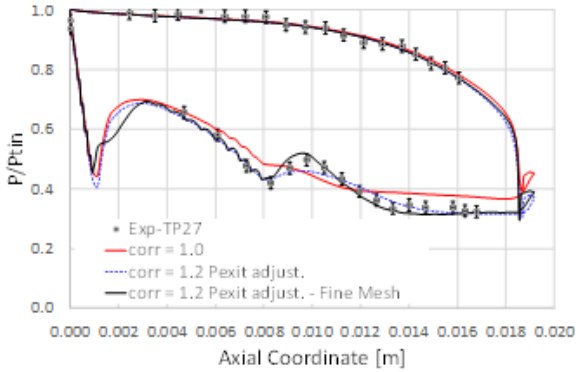

Figure 5.8: Effect of the mesh refinement (TP27, 1C14SEP9).

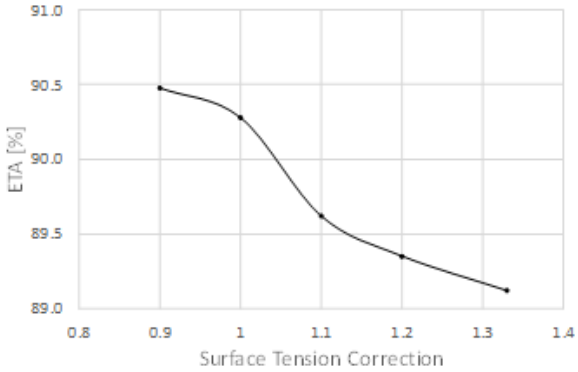

Figure 5.9: Effect of the tension correction on bladerow efficiency (TP27, 1C14SEP9).

range $1.25 - 3.25$ and inlet temperatures from $35K$ superheated to $15K$ supercooled. The calculations have been performed with and without tension correction, in order to show the correction effect at different pressure ratio.

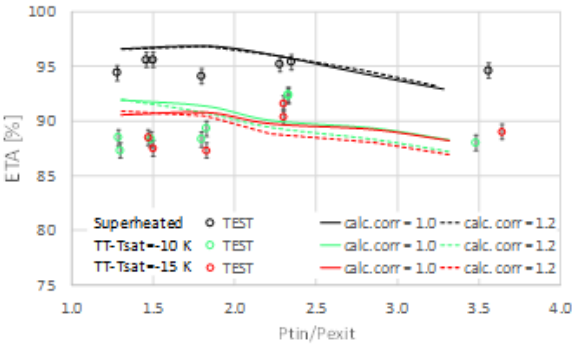

Figure 5.10: Test and calculated data w/ and w/o correction.

The comparison between calculated values and experimental results, reported in Figure 5.10, shows that the model correctly reproduces the drop of the efficiency caused by the condensation start. However, it is also evident from the comparison plot that at low Mach number, i.e. low expansion ratio, there is a significant mismatch between numerical results and test data. Increasing the surface tension by 20% as suggested by the previous discussion on blade pressure distribution, does not help a lot. Additional sensitivity tests on the parameters of the droplet growth Equation 2.39 are presented in Figure 5.11. To this purpose, one case is selected among the points at low pressure-ratio reported in Bakhtar et al. [43], namely the case 3C3JL90 with supercooled inlet steam ($T_{sat} - TT = 11.5K$). However, the results shown in Figure 5.11 do not suggest any obvious way to

improve the matching with the experimental data. Such a difficulty is not new in cascade simulations (see Starzmann et al.[46] and Grübel et al. [47] for example), and it could be related, on top of some limits of the condensation model, also to the uncertainty in the measure of the inlet conditions of the steam.

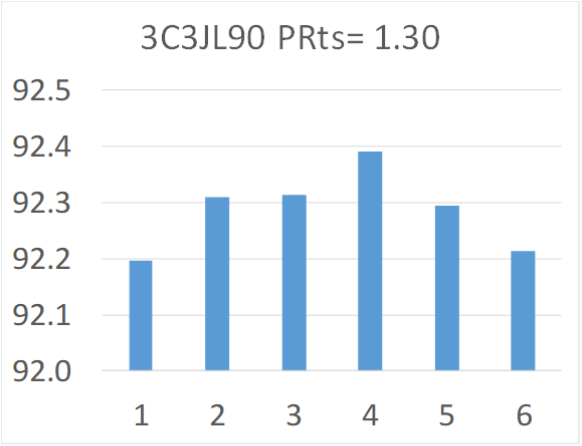

1	2	3	4	5	6
ALPHA=0	ALPHA=9	ALPHA=0	ALPHA=0	ALPHA=9	ALPHA=0
BETA=0	BETA=2	BETA=2	BETA=2	BETA=2	BETA=2
Qc=1	Qc=0.1	Qc=1.0	Qc=1.0	Qc=1.0	Qc=1.0
Corr=1.1	Corr=1.0	Corr=1.0	Corr=1.1	Corr=1.0	Corr=0.9

Figure 5.11: Sensitivity to the parameters of Young Equation 2.39.

5.1.2 THE CASES WITH WET STEAM

In order to test the new methodology in a wide range of conditions, the data at design expansion ratio from Bakhtar et al. [44] have been used to extend the analysis and to include some cases with wet steam at the inlet of the cascade. A summary of the conditions for the run extracted from Bakhtar et al. [44] is reported in Table 5.1. Case A is superheated, and no nucleation is present. Case B has saturated steam at the inlet, and the steam is wet at the exit. Case C and D have 1% and 1.8% of wetness at the inlet respectively, in the form of relatively large droplets. Case E and F have 1.4% and 1.6% of wetness at the inlet respectively, in the form of relatively small droplets. A correction factor equal to 1.20 for the surface tension has been used in this section. In order to show the impact of the nucleating steam, it is possible to compare the case A with the case B. By looking at Figure 5.12 it is possible to locate the bump in the pressure distribution on the blade surface which is the evidence of the nucleating steam. A significant mismatch between the measurements and the numerical results can also be seen on the aft part of the suction side, and more generally, in the exit pressure. This is due to the fact that in the original publication only the pressure ratio intent is reported, and not the measured one.

An adjustment of the exit pressure, similar to what presented in Figure 5.7, would reduce the mismatch, but it is not considered necessary from the point of view of the condensation losses. In this situation, the losses related to the nucleation are very high. However, when the steam at the inlet is already wet, the losses due to the steam condensation can be different. This happens if the surface of the droplets at the inlet is large enough to suppress a second nucleation of the steam. In order to show this, the cases A, C, and F are compared and the differences in the

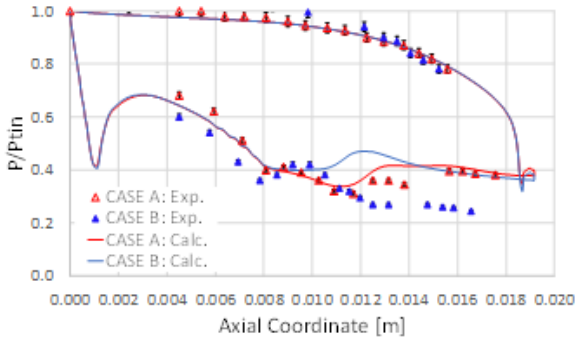

Figure 5.12: Comparison between numerical and test values: cases A and B

pressure distributions are discussed. As for the cases F and C the combination of inlet wetness and droplet radius results with a number of droplets per unit volume N_d equal to $1.2E{+}17[m^{-3}]$ and $3.7E+15[m^{-3}]$ respectively, with an area density β_d equal to $1120m^{-1}$ and $242m^{-1}$.

As for the case F, characterized by a larger area density, the losses are not due to the reversion to equilibrium of the steam. Instead, the losses are caused by the heat exchange with a tem-

CASE	**Inlet Wetness**	**Inlet droplet radius** $\cdot 10^6[m]$	P_{Tin}/P_{sout}
A	superheated	–	2.36
B	0.000	–	2.32
C	0.010	0.145	2.33
D	0.018	0.150	2.37
E	0.014	0.050	2.36
F	0.016	0.055	2.32

Table 5.1: Conditions for the analysis of the wet cases of the Bakhtar's cascade.

perature difference between the droplets and the steam vapour. This temperature difference, caused by the steam vapour supercooling, is the driver for the droplet growth and the cause of the so-called thermodynamic relaxation losses. This effect is evident when case A and case F are compared. In this case, in fact, the presence of small droplets can suppress the secondary nucleation and the related pressure knee on the suction side (see Figure 5.13).

The situation is slightly different in Figure 5.14, where the case A and case C are compared. In fact, the larger droplets of case C can only partially mitigate the effects of the supercooling of the steam, because they provide a smaller area density. The result is a secondary nucleation, which is evident in Figure 5.14 because of the knee in the pressure distribution on the suction side.

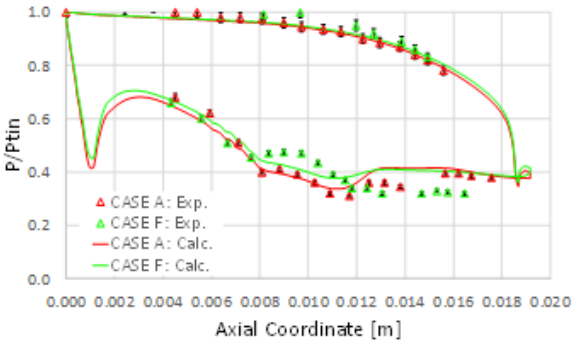

Figure 5.13: Comparison between numerical and test values: cases A and F

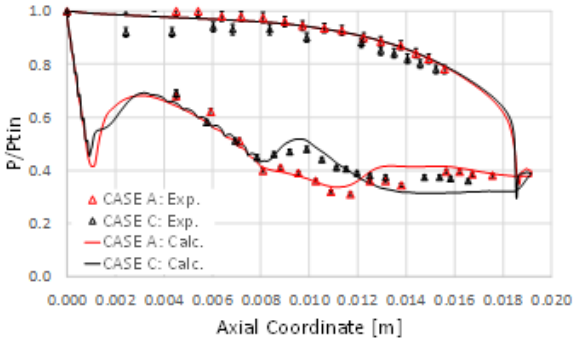

Figure 5.14: Comparison between numerical and test values: cases A and C

5.2 COMPARISON WITH CORRELATIONS

As already explained, the losses due to nucleation and thermal relaxation are very different in values. In order to clarify these differences, the values of the losses caused by these two processes have been deduced from the results already presented. This has been done in terms of the efficiency deltas. This means that for each wet or nucleating run a corresponding dry condition has been selected and the differences in efficiency have been evaluated. The obtained values are shown in Figure 5.15, together with the Bauman line.

It can be seen that the points from the nucleating cascade in subsection 5.1.1 and the ones from the wet cascade in subsection 5.1.2 points are clustered in different region of the graph, which is a first hint of the fact that the loss mechanisms are different.

It is a traditional approach (see Guo et al. [48]) to distinguish

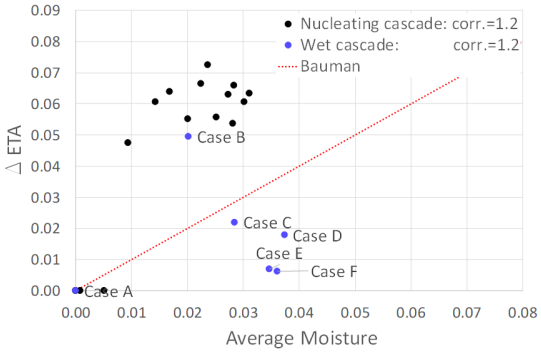

Figure 5.15: Efficiency drop vs average moisture.

between nucleation and thermodynamic relaxation losses and use different methodologies to estimate them.

As for the nucleation losses, the numerical results in subsection 5.1.1 obtained from the analysis of the nucleating cascade of Bakhtar et al. [42] are used. In order to show the effects of the nucleation, the nucleating cases are compared with their corresponding dry cases by using the outlet-to-inlet growth of entropy, expressed in non-dimensional form $\Delta s/c_p$. The difference between the values of $\Delta s/c_p$ of the nucleating cases and their corresponding dry cases is shown in Figure 5.16. As a theoretical estimate, an equation is derived from the Equation 2.45 under the assumption that the exit moisture Y_{out} is equal to the equilibrium moisture Y_{eq} quoted in the equation. The obtained equation is shown below:

$$\frac{\Delta s}{c_p} = -ln\left(1 - \frac{LY_{out}}{c_p T_{sat}}\right) - \frac{LY_{out}}{c_p T_{sat}} \tag{5.1}$$

and is added in Figure 5.16 for comparison.

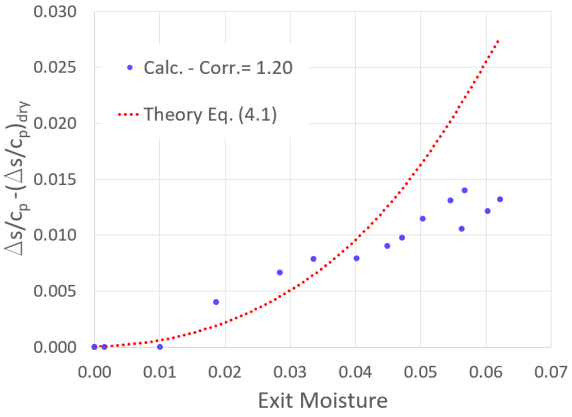

Figure 5.16: Nucleation losses: comparison between numerical and theoretical estimates.

The comparison between the theoretical curve Equation 5.1 and the non-dimensional entropy variation obtained from calculated values is shown in Figure 5.16. It can be observed from the comparison that at low level of exit moisture, there is a good agreement between the CFD results and the Equation 5.1. However, when the exit moisture gets higher than 4%, the theoretical curve from Equation 5.1 overestimates the effect of the nucleation. By comparing the maximum supercooling achieved for the considered cases it is possible to observe the cases from a different point of view. For example, in Figure 5.17 a case with 4% of exit wetness is compared with another with 6%. The two cases have the same pressure ratio, which means that the inlet supercooling is higher for the 7% case. As can be seen, the maximum supercooling for the two cases is the same, while the nucleation region, shown in Figure 5.18, is located almost in the same place. From Equation 2.40 it is easy to show that with supercooling equal to $44K$ the equivalent wetness is about 4%.

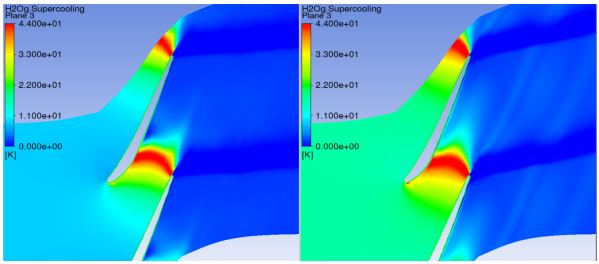

Figure 5.17: Supercooling for the 4% and 6% cases.

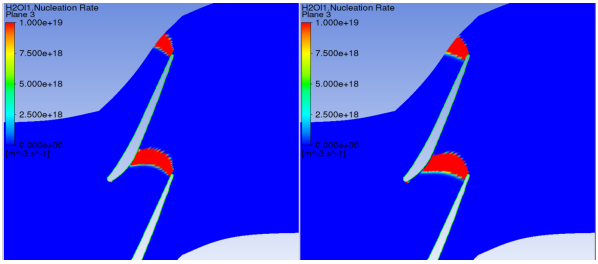

Figure 5.18: Nucleation rate for the 4% and 6% cases.

This also means that in the two considered cases an amount of wetness around 4% is formed during the nucleation, and that the wetness in excess to 4% is formed through the growth of the droplets. Looking at the Figure 5.19, it can be seen that all the wetness is formed between the line of maximum supercooling of $44K$ and the isoline of $4K$. In terms of losses, this means that when the expansion is beyond the 4% threshold, a mechanism different from the one described by equation Equation 5.1 is acting. As for the thermodynamic relaxation losses, the pressure distributions in subsection 5.1.2 shows the different behaviour of the cases depending on the size of the droplets. Elaborating the numerical results, it is possible to see how the droplets entering the cascade domain affect the losses too. In

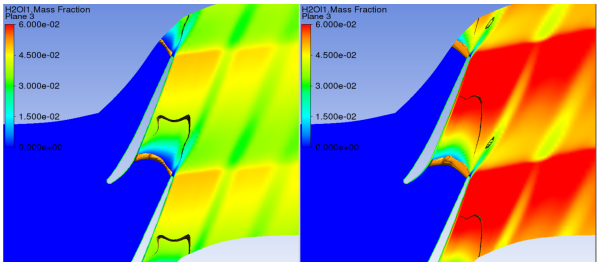

Figure 5.19: Wetness distribution and maximum supercooling for the 4% and 6% cases.

order to extract the wetness losses from the numerical results, the increase in the non-dimensional entropy growth is used like in the nucleating case. However, here different forms of the entropy balance are used to get a theoretical estimate of the losses due to the expansion of a supercooled wet steam. The first one is the Equation 2.58, used in conjunction with value of the supercooling obtained from the calculations. The second one is the Equation 2.59. The third one is the Equation 2.54. The numerical calculations obtained with a correction factor for the surface tension σ equal to 1.20 are shown in Figure 5.20, together with the values of the wetness losses estimated using Equation 2.57, Equation 2.59, Equation 2.54. As a reference, Equation 5.1 is added in the plot as well. In the plot, cases A and B represent the superheated case and the nucleating case already analysed. The cases E and F, with small droplets, do not present nucleation, as previously shown in Figure 5.13. Therefore, their loss level is very close to the one predicted by Equation 2.58. As for the case C and D, they represent an intermediate condition between the nucleating flow (i.e. case B) and the wet flow (i.e. case E and F), for which no simple correlation exists. Therefore, looking at the Figure 5.20 it is apparent that Equation 2.58 can

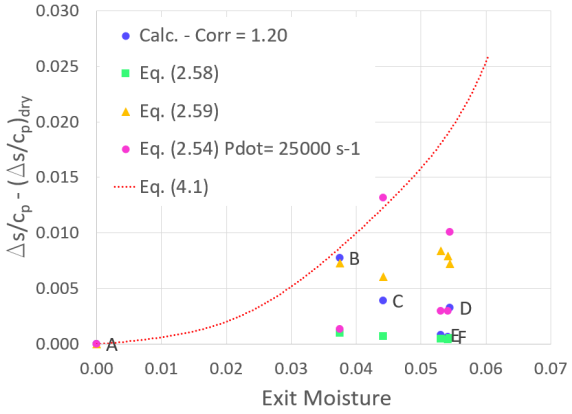

Figure 5.20: Thermodynamic relaxation losses: comparison between numerical and theoretical estimates.

be used to estimate the losses due to the heat transfer between the droplets and the vapour, but only in those cases where the temperature difference between the phases is nearly constant. As for Equation 2.54, it is worth to spend some words to explain the disappointing match in Figure 5.20. In Figure 5.21 the expansion rate for the case C is shown. It can be observed that the expansion rate $\dot{P}$ varies a lot across the cascade, and therefore estimating the proper value to be used in Equation 2.54 is generally difficult. As the maximum value is $50000s^{-1}$, an average value equal to $25000s^{-1}$ is used in the Figure 5.20. Looking for a better match, several tests have been done changing the value of $\dot{P}$ used in Equation 2.54. From the results shown in Figure 5.22 it can be shown that a better match can be obtained by using a value of $\dot{P}$ around $10000s^{-1}$. Such a value is close to the low end of the range of $\dot{P}$ in Figure 5.21, and this suggests that the thermodynamic relaxation losses could depend more on the flow evolution in the gap between the bladerows than in the bladed

region. However, understanding if the droplet laden flow could sustain a certain super-cooling without causing a secondary nucleation still remains the major problem in the application of Equation 2.54.

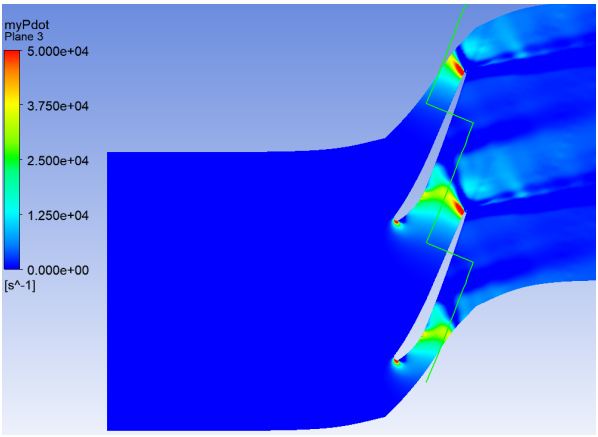

Figure 5.21: Expansion rate: case C.

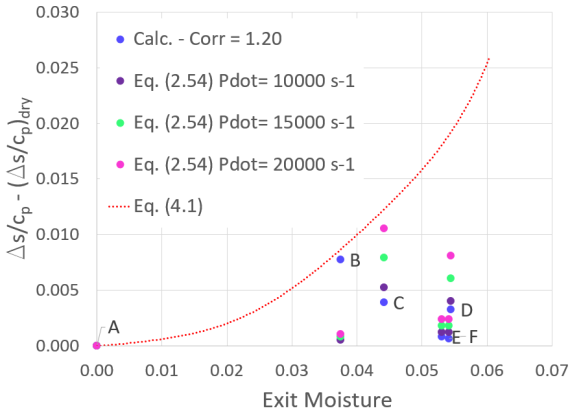

Figure 5.22: Thermodynamic relaxation losses from Equation 2.54 at varying $\dot{P}$.

Chapter 6

ANALYSIS OF A LP SECTION

In this chapter, a low-pressure section of recent development is analysed using two different methodologies. The first one consists of a conventional methodology, where the two phases are assumed to be in equilibrium (ES). The second one, labelled as Non-Equilibrium Steam (NES), consists of the two-phase methodology previously described and validated in chapter 4 and chapter 5, where planar nozzles and cascade geometries are considered. The results obtained with the two methodologies are compared with the experimental data in terms of total-to-total efficiency. Different operating conditions are considered to this purpose, with different wetness at the exit and different pressure ratios, in order to show clearly the loss trend for different level of exit moisture. The numerical results are compared with the experiments and with some correlations available from open literature or built on proprietary data.

6.1 THE LOW-PRESSURE SECTION

A lot of research papers have been published over the years to clarify the many aspects of the two-phase flow in the steam turbines. Perhaps, the one that helped to fill the gap between the numerous tests done on plane nozzles, the theoretical aspects of the condensation physics and a systematic comprehension of the loss mechanisms related to the wetness in the flow is given in Gyarmathy [13], where a systematic framework of all the wetness losses can be found. The most relevant ones in terms of performance are grouped as follows:

- Nucleation losses
- Thermodynamic relaxation losses
- Interphase drag losses
- Braking losses
- Pumping losses

The methods from Computational Fluid Dynamics (CFD) entered into the world of non-equilibrium steam flow in the 80's, initially with throughflow methods (Yeoh et al. [33]), and then with 2D (Bakhtar et al. [34]) and 3D calculations (Liberson et al.[36]). Designers have exploited this new tool to improve the turbine performance accounting for non-equilibrium effects. Recent publications dealt with the analysis of part-span connectors for LP rotating blades (e.g. Hafele et al. [49], Mistry et al. [50], Ferhatoglu et al.[51]), supersonic tip concepts (e.g. Sreedharan et al. [52]), exhaust system optimization (Diurno et al. [53]) or even complete LP modules (e.g. Starzmann et al. [46]). However, Young et al. [54] and, more recently, the International Wet Steam Modeling Project (Starzmann et al. [12] have shown

that a considerable uncertainty in nucleation theory and droplets growth law exists, and for this reason no common modelling approach exists as well.

6.2 THE TEST RIG LAYOUT

The recent developments of new LP sections of steam turbines, like the ones in Senoo et al. [55], Novak et al. [56], Brunn et al. [57], and Hoznedi et al. [2], all show that in the industrial practice a testing campaign is needed to get a final assessment of a new steam turbine, as it is generally felt that the analytical tools are not yet reliable enough to guarantee performance or structural integrity over the full range of operating conditions. For this same reason, the turbine that is considered here was tested in 2007 and 2009 in the Low Pressure Development Test vehicle (LPDT) in the General Electric campus located in Schenectady (NY). The test rig layout is designed to test a LP section over a wide range of operating conditions, as is shown in Figure 6.1.

For the calculation of the performance of sections and stages or of total exhaust losses, temperature and pressure probes are placed throughout the flow path and within the hood. An inline torque meter provides a measurement of the power output from the tested turbine stages, while a load-absorbing water brake gives a second measurement as further check. On the endwalls, the test vehicle was instrumented with pressure taps, in order to measure static pressures, while on the leading edge of the nozzles of each stage, total temperature and pressure probes are installed. At the inlet of the exhaust hood, the total pressure and temperature are measured at five radial locations adopting five rakes equally spaced in the annulus. For a more accurate description of the flow field, additional measurements are performed by

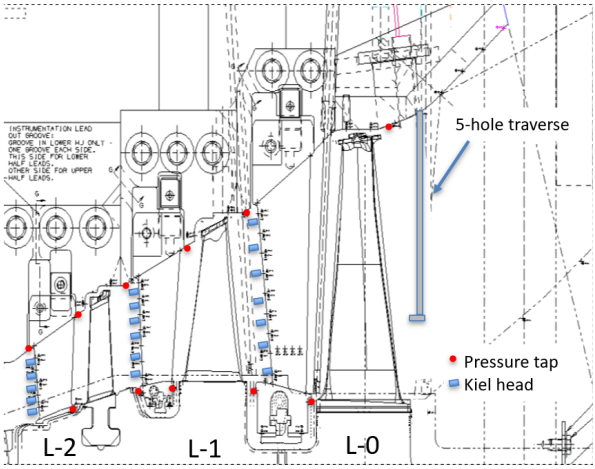

Figure 6.1: Test vehicle layout with instrumentation

means of two traverses equipped with standard five-hole probes.

Additional details on the test bed can be found in Basirico et al. [58], Piraccini et al. [59] and Maceli et al. [60], while some of its main capabilities are summarized in Figure 6.2.

Although the test campaign was conducted exploring the expected operating range of the LP section by changing systematically the rotating speed, the inlet and exit conditions, in this research only the experimental data at the design rotating speed and mass flow are considered. In order to validate the performance prediction, the analyses are done over the range between the conditions of limit load and windage for the last stage. Among the considered ones, there are three operating conditions at the design pressure ratio and mass flow rate, but different moisture content at the exit that are analysed in details to show clearly the effects of the moisture on the performance and on the aerodynamics of the LP stages. They are labelled as G6, B6, D4 in the following discussions, and have an exit

LPDT- General Description of Facility Capabilities	
Low Pressure Development Turbine (Schenectady)	
Description	**Capability**
Turbine Size:	
Scale	1/3
Stages	Typical 4
Power	300 KW - 17 MW (23,000 HP)
LSB Size	Scaled to 62"
Steam Parameters:	
2 Boilers	20 ~290,000 PPH
Max Steam Temp	~ 180 - 650 [F]
Max Steam Pressure	415 psia
Turbine inlet pressure	7-80 psia
Rig Speed Capability:	Train Max 12,000 rpm
Turbine bearings	12,000 rpm
Small torquemeter (HP end)	14,000 rpm
Large torquemeter (LP end)	14,000 rpm
Kahn 106 small brake (HP end)	14,000 rpm
Kahn 406 large brake (LP end)	12,000 rpm
Water Box Condenser	
Exhaust Pressure	0.3 - 11 psia
Heat Rejection	River Water
Other:	
Turbine Control	Mk VI
BOP Control	PLC
Dual Pipe Inlet, Single Exhaust, Hood within a Hood Construction	Na
Instrumentation & Measurements:	
Pressures (rig only) - Scannivalve	600 leading edge and wall
Temperatures (rig only) - TruTemp	400 leading edge and wall
5 Traverse probes (LC Smith actuators)	Inlet, Intra, exit L0 stage
2 water brakes/Dynamometers - Kahn	3 MW + 14 MW
2 inline torque meters - Torquetronics*	+/- 0.1% FS
2 flow meters (steam & condensate sides)*	+/- 0.25% cal'd range
Facility Instrumentation	Assorted

Figure 6.2: Main characteristics of test facility

moisture respectively equal to 0%, 5%, and 8%.

In the present research only a set of the experimental data available from the test campaign will be used. The data that will be used are:

- 4 rakes at vane leading edge for total pressure
- 2 rakes at vane leading edge for total temperature
- Pressure taps for ID and OD
- 2 inline torque-meters
- Bearing losses measured via oil heat balance
- ASME PTC6 Flow nozzle as flow meter
- Traversing system at the outlet plane

The experimental value of the efficiency is obtained combining the measured values of the torque, speed, steam mass flow rate, inlet enthalpy and total pressure at the exit, as per equation below:

$$\eta_{tt} = \frac{\mathbb{T}\omega + Loss_{bearing}}{\dot{m}\left(H_{Tin} - H_{T_{out}}^{ss}\right)} \tag{6.1}$$

6.3 THE NUMERICAL SETUP

The setup of the case is similar to the one previously used for subsection 4.1.1, subsection 4.1.2 and chapter 5. This means that all the calculations have been performed using the commercial code ANSYS CFX v.18. Two different series of calculations are reported here.

The first one is obtained using a conventional methodology, where the two phases are assumed to be in equilibrium. This

series is labelled as Equilibrium Steam (ES) and is obtained using the model homogeneous binary mixture (see [40]).

The second one, labelled as Non-Equilibrium Steam (NES), is obtained using the two-phase methodology previously described and validated in chapter 5, where planar nozzles and cascade geometries are considered. In line with the findings of the previous chapter 5, a correction equal to 1.2 is used for the analysis of the LP section.

The calculations are performed with a second order spatial discretization scheme. For all analysed models the following are applied:

- Steady state solution
- SST turbulence model with Kato Launder limiter
- IAPWS steam tables as working gas model
- Mixing plane between blade rows

All the calculations have been converged with a final physical time step equal to 1.e-6 seconds.

The selected approach doesn't include the effects of the coarse wetness, of the deposition and the detachment of the droplets from the blade walls. Braking losses and pumping losses are also excluded out of the present research. In terms of performance, this represents a minor problem because of the low wetness level considered. Generally speaking, however, including these aspects in the model it is of great interest for it would provide the designers some very useful pieces of information about the conditions where the LP section stages operate, especially from the point of view of the erosion risk to which the rotating blades are subject. In a preliminary part of the activity (see Bellucci et al. [61]), a simple model of shroud leakage is used, where the effects of the

leakages are accounted for with a source-sink approach applied at the cavity/mainstream interface. In the present research, including the effects of the leakages has required to model the real geometry of the seals. This is deemed necessary as the leakage flows at the outer diameter (OD) for the shrouded rotating blades or at the inner diameter (ID) for the fixed nozzles have a significant role in the overall turbine performance. To this purpose, Workbench v.18 has been used to build the computational meshes. All computational meshes are tetrahedral with 14 inflation layers. The thickness of the first layer is 0.0001mm. The thickness of the first layer is small enough to keep y^+ below one on all the solid walls. Compared to a previous research (Bellucci et al. [61]), adding the details of the seals and refining the mesh to capture the nucleation front increased the mesh to 40.5 M of cells. In the last decade, several publications have focused on the interaction between the main flow and the leakage flows (Wallis et al. [62], Pfau et al. [63], Rosic et al. [64]). In order to capture the effects of the interaction between the leakages and the mainflow, attention must be paid to the position of the interface planes between neighbouring blade rows. Therefore, the planes are placed in a way that change of reference occurs at the first or second sealing tooth, so that the interaction between the main flow and the leakage flows re-entering the flow path is preserved (see Figure 6.3). In order to avoid reflections, the pressure boundary condition is set downstream the L0 Bucket exit measurement plane. The proper radial distribution of pressure used as boundary condition at the Outlet plane is obtained by targeting the radial profile of the measured static pressure at the L0 Bucket exit.

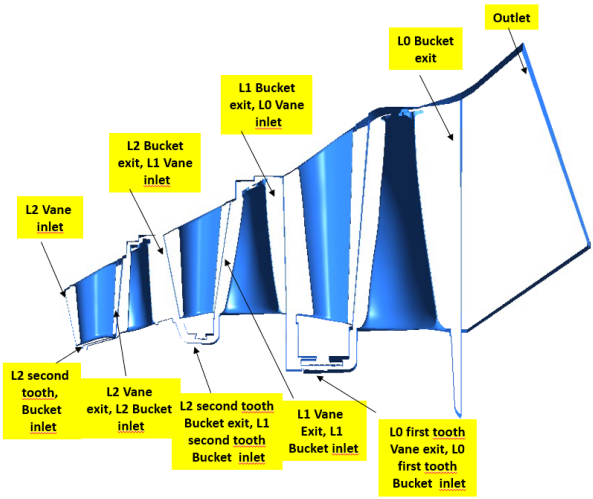

Figure 6.3: View of the computational domain.

6.4 THE NUMERICAL RESULTS

Using the numerical approach so far described, the LP section is analysed, and the obtained efficiency curve is compared with the experimental curve. In the already mentioned research Bellucci et al. [61], the CFD data are corrected using the approach described in Guo et al. [48] to overcome the limitations of the CFD code.

The research shown in this chapter is carried out in a different way. In order to show the effects of the non-equilibrium behaviour of the steam, two series of calculations are considered.

The first one is obtained using a conventional methodology, where the two phases are assumed to be in equilibrium. This series is labelled as Equilibrium Steam (ES) and is obtained using the model homogeneous binary mixture (see [40]).

The second one, labelled as Non-Equilibrium Steam (NES), is

obtained using the two-phase methodology previously described and validated in chapter 4 and chapter 5, where planar nozzles and cascade geometries are considered.

6.4.1 COMPARISON TO THE TEST DATA

The results obtained with the two methodologies are compared with the experimental data in terms of total-to-total efficiency with the purpose to show their different capabilities. The results obtained with the ES approach are shown in Figure 6.4, while the ones obtained with the NES methodology are shown in Figure 6.5. The results shown in Figure 6.4 are generally consistent to the ones obtained using a different CFD code (namely the TRAF code) in Bellucci et al. [61]. Also, in this case, a mismatch in the range of 2 efficiency points is found at the dry conditions G6.

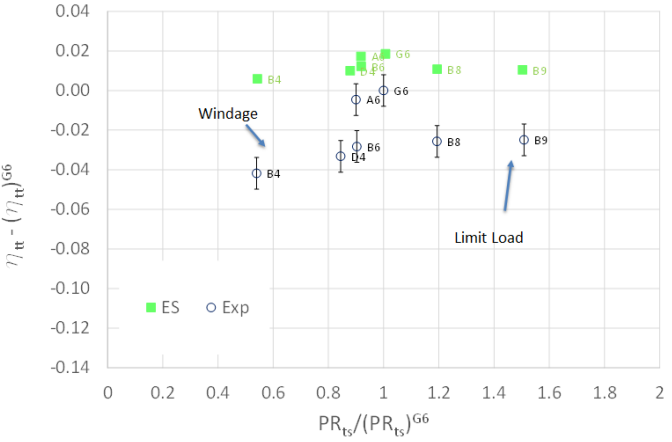

Figure 6.4: Equilibrium Steam: Total-to-total efficiency vs PRts.

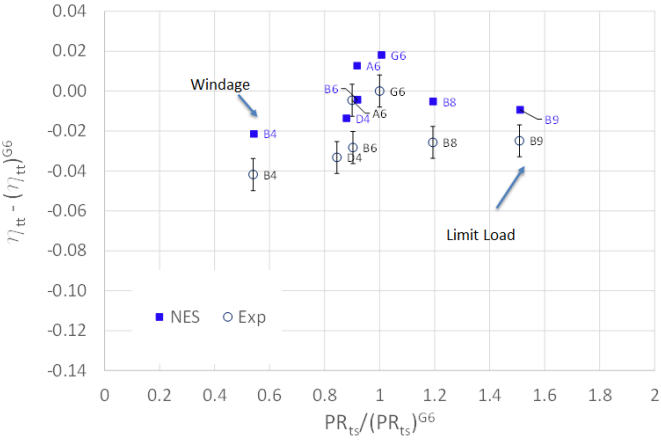

Figure 6.5: Non-Equilibrium Steam: Total-to-total efficiency vs PRts.

On the other hand, the results in Figure 6.5 are in good agreement with the experimental data, and reproduce with accuracy the shape of the efficiency curve, while in the case of Figure 6.4 the ES results are more flat compared to the experiments. A detailed comparison between the test data and the numerical results is done in terms of spanwise distributions considering the dry test condition G6. In Figure 6.6 and in the following Figure 6.7 and Figure 6.8, each label of the experimental data refers to a specific angular position of the pressure/temperature rakes, measured in the counter-clockwise direction with respect to the right-hand side of the horizontal flange of the machine. In Figure 6.6 the total temperature and pressure at the inlet of the L1 stage are shown. It can be seen that the agreement is good in qualitative terms, but the total pressure distribution calculated by the CFD is in the lower range of the experimental measurements. In Figure 6.7 a similar set of data is shown for the inlet of

the L0 stage: it can be seen that in this case the agreement is less good, especially in terms of total pressure. This apparent failure to match the experimental measurements has to be judged in the light of the efforts required to measure the pressure with steam as working fluid. In fact, during the tests the steam tends to condensate into the pressure lines, thus causing the build-up of water legs inside them. A special system is used to purge the lines and

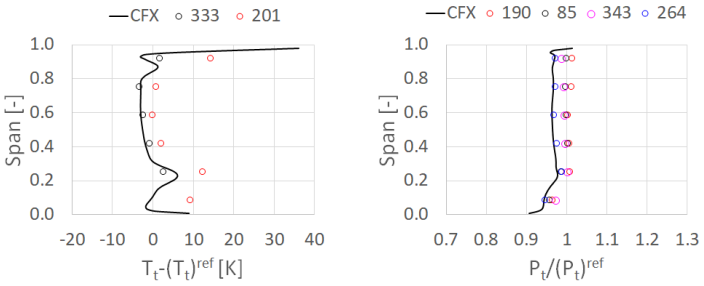

Figure 6.6: Radial distributions at the L1 stage inlet: G6 condition.

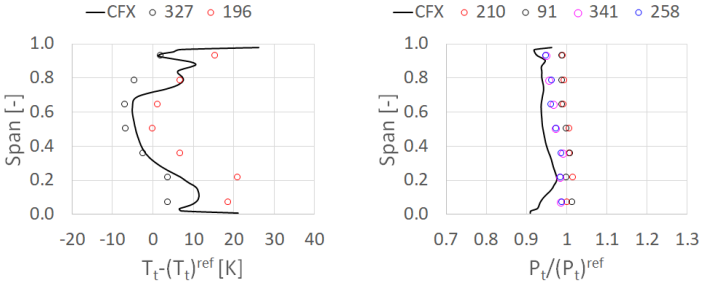

Figure 6.7: Radial distributions at the L0 stage inlet: G6 condition.

heat them during the tests to avoid this phenomenon. However, the difficulties in the tests still remain, as it is demonstrated by the significant differences in the pressure profiles measured by the different rakes. Other reasons for such a mismatch could be related to some limits of the two-phase differential equations Table 3.1 and, in particular, to the frozen pressure assumption outlined in subsection 3.1.1. Finally, in Figure 6.8 the comparison between the numerical results and the test data is shown in terms of total pressure and temperature, and in terms of swirl. The agreement in terms of total temperature distribution and in terms of swirl are especially good, because of the detailed modelling of the gap geometry at the tip of the L0 bucket. However, the CFD shows a clear tendency to underestimate the measured total pressure. This is in line with the fact that the efficiency of the LP section is overestimated, as already shown in Figure 6.5. The static pressure distribution is also reported, showing how the outlet boundary conditions is correctly reproduced, at least in terms of average quantities.

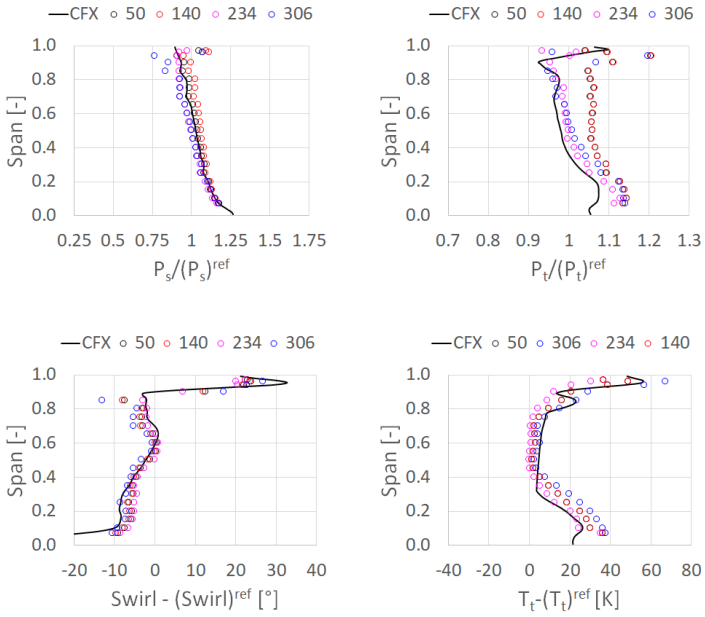

Figure 6.8: Radial distributions at the L0 stage exit: G6 condition.

The agreement between the numerical results and the test data is generally good, as shown in Figure 6.5. However, a better view of the predictability of the two methodologies is achieved by using the parity plot in Figure 6.9, where the numerical results are plotted against their corresponding experiments.

In the plot, several data sets are shown:

- the numerical results obtained with the NES methodology
- the numerical results obtained with the ES methodology
- the results obtained using the 1D code of Guo et al. [48] and outlined in Equation 2.51
- the results obtained by applying the moisture losses as per the 1D code and Equation 2.51 to the results obtained from ES.

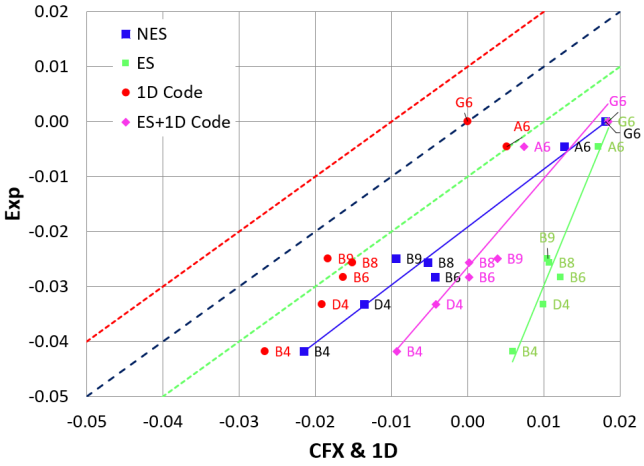

Figure 6.9: Parity plot of total-to-total efficiency.

In the plot the parity line is also added together with two lines that show the lower and upper limits of the tolerance interval. Looking at the plot in Figure 6.9, it can be seen the significant improvement in the predictability achieved with the new methodology NES. In particular, the Non-Equilibrium Steam methodology allows for an improvement in the predictability as high as 2 efficiency points in most of the considered operating conditions with respect to the more conventional ES approach. The benefit in terms of predictability in the order of 1 efficiency point is also noticeable if we consider the ES results corrected for the wetness losses, which is the industrial practice before NES. As for the comparison between the NES and the 1D code, the values obtained using the same inhouse performance code used in Bellucci et al. [61] are also reported in the plot and labelled as $1Dcode$. The performance code reproduces quite well the experimental data, generally within the experimental uncertainty. This should not be a surprise, given the fact that the 1D code has been tuned to match the test data at the G6 test condition. The tuning has been done on a stage-by-stage basis by using the measurements of total pressure and temperature available from the instrumentation on the vane leading edge and at the L0 Bucket exit plane. In order to better understand the mechanisms behind the difference predictability of the four methods, additional investigations are carried on.

6.4.2 THE WETNESS LOSSES

The effect of the wetness losses can be deduced by subtracting the NES values from the corresponding ES results. The obtained deltas represent the efficiency loss caused by the combined effects of the condensation, of the thermal relaxation losses and of the shift in the operating conditions on the stages. The obtained values are compared in Figure 6.10 with the values previously used to correct the CFD results in Bellucci et al. [61], used in the same way also for the Figure 6.9, and labelled as 1D code in the plot. It is interesting to observe that the trend of the NES results is different from the estimates obtained via correlative approach. In particular, the plot shows that according to NES calculations the wetness losses reach a 2.5 efficiency points for the test point D4, while the 1D code estimates a much lower value of 1.5 points. This shows how different methodologies can give the same final efficiency estimate and have at the same time a different split of the losses.

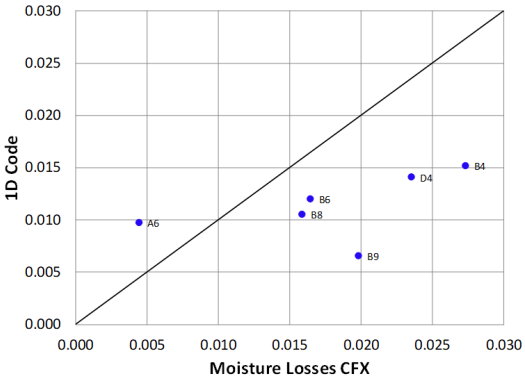

Figure 6.10: Parity plot of wetness losses.

The method discussed above is not obviously applicable when experimental data are of concern. In that case, the way commonly used to obtain the wetness losses is derived by the classical approach of Bauman [7] and improved over the years by many researchers, like Miller et al. [27] and Kreitmeier et al. [25]. Following this approach, the efficiency of a given operating condition with wet steam at the exit is compared with the efficiency of a corresponding condition with dry steam at the exit, and the wetness losses are obtained by subtracting the second from the first. In the original publication, Bauman [7] was able to fit the experimental data against the average wetness of the expansion by using $\alpha_B = 1$. For the cases considered in the present paper, Bauman's rule can be written as:

$$\frac{\eta_{tt}^{(G6)} - (\eta_{tt}^{(NES)}}{\eta_{tt}^{(G6)}} = \alpha_B \frac{Y_{exit}}{2} \frac{H_{Twp} - H_{Texit}}{H_{Tin} - H_{Texit}} \tag{6.2}$$

The term $\eta_{tt}^{(G6)} - \eta_{tt}^{(NES)}$ is calculated using the data obtained from the CFD results, the 1*Dcode*, and the experimental data of the test points B6 and D4, whose efficiencies are subtracted from the efficiency of the test point G6. The obtained wetness losses are shown in Figure 6.11. It can be seen in the plot that, the trend of the 1D code is different from the others: in this case, the NES methodology estimates an efficiency drop equal to 3.5 efficiency points, in line with the test data, while the 1D code estimates only 2 efficiency points. The attentive reader will not have missed the fact that deducing the wetness losses using these two methods provides very different results: for the D4 test point we find 2.5 efficiency points in Figure 6.10 and 3.5 points in Figure 6.11. In order to reconciliate these two values, it is necessary to consider that the test points G6, B6 and D4 have different expansion lines, although their pressure ratios and mass

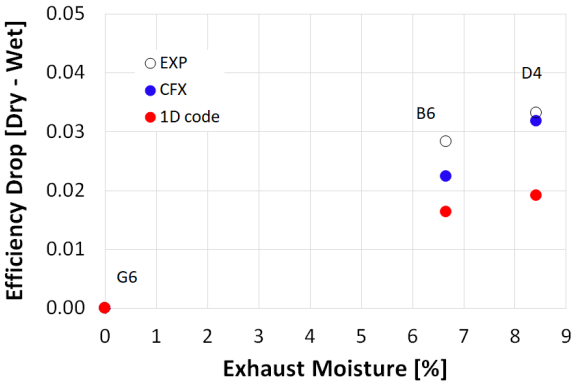

Figure 6.11: Efficiency drop at different exhaust moisture.

flow rates are similar. The relationship between G6, and NES and ES values can be written as:

$$\eta_{tt}^{(G6)} - \eta_{tt}^{(NES)} = \eta_{tt}^{(ES)} - \eta_{tt}^{(NES)} + \eta_{tt}^{(G6)} - \eta_{tt}^{(ES)} \tag{6.3}$$

The term given by the difference $\eta_{tt}^{(G6)} - \eta_{tt}^{(NES)}$ is the one shown in Figure 6.11. The term $\eta_{tt}^{(ES)} - \eta_{tt}^{(NES)}$ is the one in Figure 6.10. As for the third term $\eta_{tt}^{(G6)} - \eta_{tt}^{(ES)}$, it can be written as:

$$\begin{aligned} &\eta_{tt}^{(G6)} - \eta_{tt}^{(ES)} = \eta_{pol}^{(G6)} RH^{(G6)} - \eta_{pol}^{(ES)} RH = \\ &= \eta_{pol}^{(ave)} \left(RH^{(G6)} - RH \right) + RH^{(ave)} \left(\eta_{pol}^{(G6)} - \eta_{pol}^{(ES)} \right) \end{aligned} \tag{6.4}$$

The expansion lines of the three operating conditions are shown in the Mollier diagram in Figure 6.12, with the quality lines from 1.0 to 0.92. The corresponding reheat factors RH in Figure 6.13, change by more than 2 points.

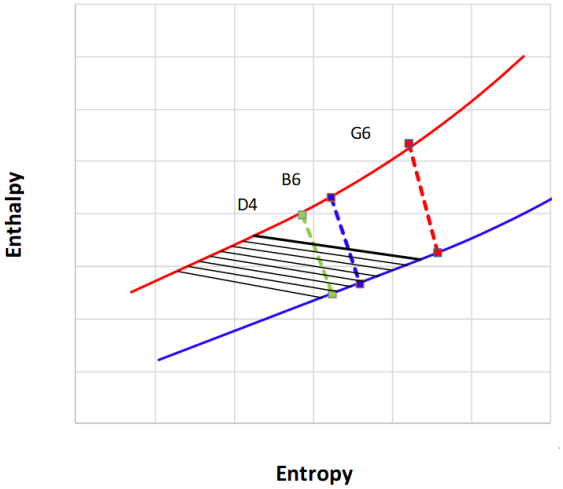

Figure 6.12: Expansion lines of the considered cases.

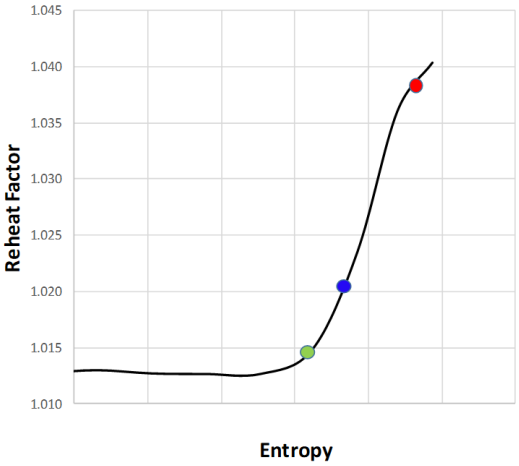

Figure 6.13: Reheat factor for the considered cases.

Therefore, the relative magnitudes of the numbers of the D4 case of Figure 6.10 and Figure 6.11 suggest, through Equation 6.3 and Equation 6.4, that the 2.5 efficiency drop due to the wetness losses and the 2 points of reduction in the reheat factor RH come together with an increase of about 1.0 points in the expansion efficiency η_{pol}. Such an adjustment is basically driven by the reduction of the stage loading that is discussed in the next section.

6.4.3 AERODYNAMIC ASPECTS

In order to show how the aerodynamic design intent is affected by the different methods used for the analysis, the pressure ratio and the load factors are discussed in this paragraph. They are, in fact, among the most important parameters used for the aerodynamic design of the stages. To show the impact of the droplet nucleation on the aerodynamics of the blades, the discussion will focus on the results obtained for the B6 and D4 test points. As already mentioned, B6 and D4 test points have different inlet temperature and different moisture level at the exit. In Figure 6.14 and Figure 6.15 the supercooling map is shown on the periodic surfaces for the B6 and D4 test points on the periodicity surfaces. In those plots, the re-entrance regions of the leakages are highlighted in order to show how these interact with the main flow and reduce locally the supercooling because of their higher temperature. This effect is clearly visible also in the subsequent Figure 6.16 and Figure 6.17, where the nucleation regions are found at the positions of the maximum supercooling of Figure 6.14 and Figure 6.15.

As expected, the nucleation region moves upstream when inlet temperature is reduced. The results show that the nucleation occurs on the L0 vane for B6, and on the L1 rotating blade for

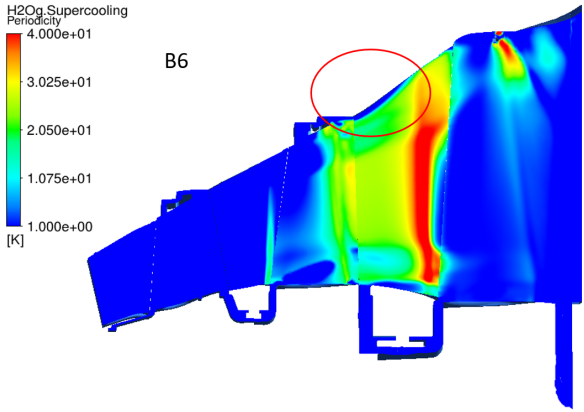

Figure 6.14: Supercooling for the B6 test point.

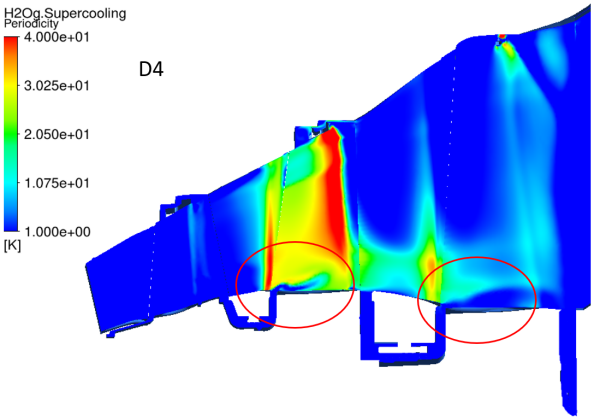

Figure 6.15: Supercooling for the D4 test point.

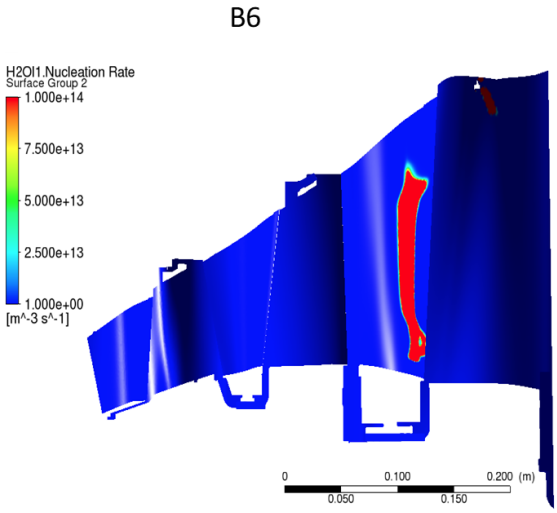

Figure 6.16: Nucleation region for the B6 test point.

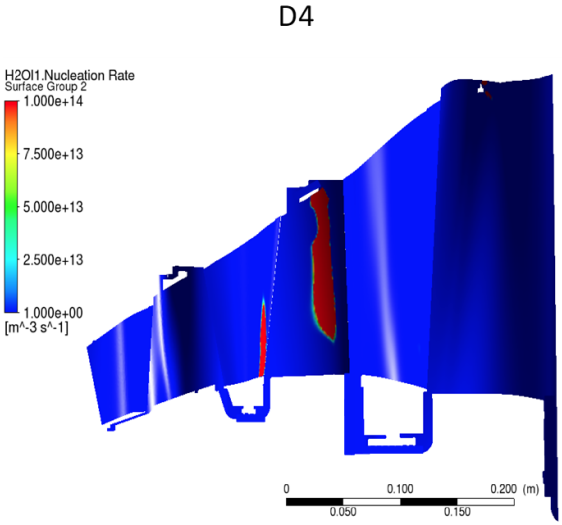

Figure 6.17: Nucleation region for the D4 test point.

D4. The position of the nucleation onset has some effects on the LP section. Among the others, the first one is that when the nucleation moves towards the L1 stage and a larger fraction of the expansion occurs in the wet region of the steam diagram, higher losses are obtained together with higher moisture at the exit. Even if this is in line with the common experience, the result is not obvious, as the wetness losses depend on the actual conditions under which wetness is formed. A second one is that the operating conditions of the stages change as the steam flow expands beyond the saturation line of the steam diagram. This is obvious in the sense that when the fluid properties of the steam change, then the aerodynamics of the stages is expected to change as well. In Figure 6.18 the total-to-total pressure ratios of the stages are shown for the selected test points, as calculated using the ES method. It can be seen in the plot that passing from G6 to D4 affects mainly L1 and L0 only, while L2 stays nearly unchanged. It seems, however, that the major impact is related to the passage between the dry G6 and the wet B6, while smaller adjustments occur for B6 to D4. At the same time, the stage load coefficients λ in Figure 6.19 reveal the dominant effect of the inlet temperature on the available enthalpy drop for the selected test points, which is the main cause of the reduction of the stage load. The results in Figure 6.20 obtained with the NES methodology show a different scenario. As for the L2 stage, no major differences are found. Also, in the case of B6 condition, the L0 and L1 stages nearly replicate the results obtained for the ES methodology in Figure 6.18. When the inlet temperature is decreased further and the nucleation front moves to the L1 rotation blades, a major adjustment occurs in the pressure split between the stages. This is due to the increase in swallowing capacity caused by the supercooling at the L1 exit. This

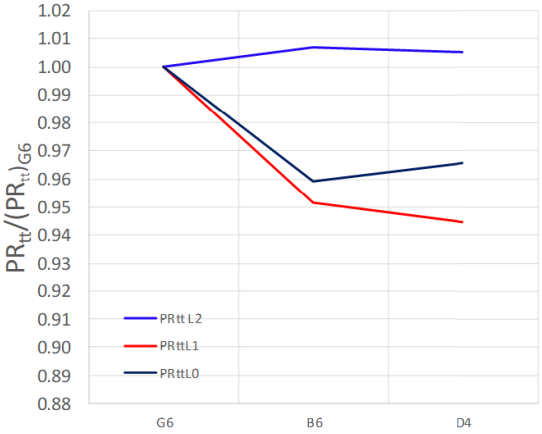

Figure 6.18: Stage Pressure ratio for different test points: ES results.

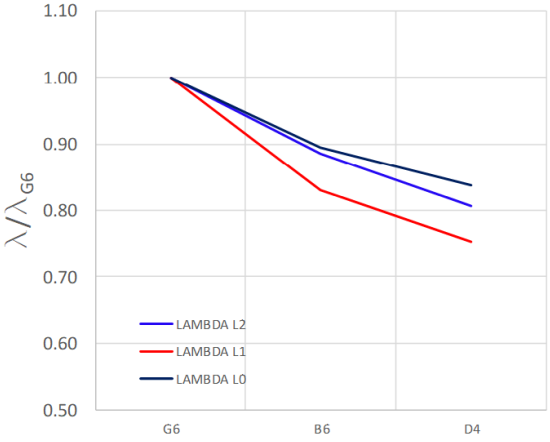

Figure 6.19: Load coefficients for different test points: ES results.

increase, discussed in Young [65] and Kreitmeier et al. [25], is also present in the results reported in Starzmann et al. [26], and it appears to be one of the main causes for the stages to operate in off-design condition. Other differences in the case of NES calculations can be observed in Figure 6.21, where the cascading effects of the adjustments in the pressure split are shown for the stage load λ: in fact, in the plot it is evident how reducing the inlet temperature from B6 to D4 is moving part of the workload of the L0 stage to the L1 stage. In order to understand the extent of these adjustments, the pressure distributions of the blading of L1 and L0 are analysed at the midspan in Figure 6.22 and Figure 6.23 for test point B6 and D4 respectively. The plots show the comparison between the ES and the NES results. As expected, the droplet nucleation affects the pressure distribution of the L0 stationary vane, and the heat released by the condensing steam reduces the velocity peak on the suction side of the

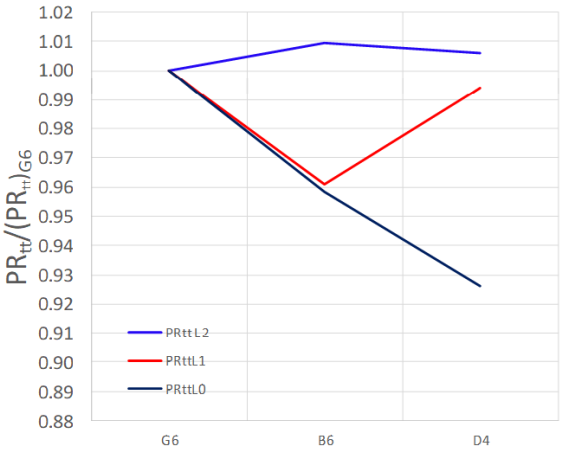

Figure 6.20: Stage Pressure ratio for different test points: NES results.

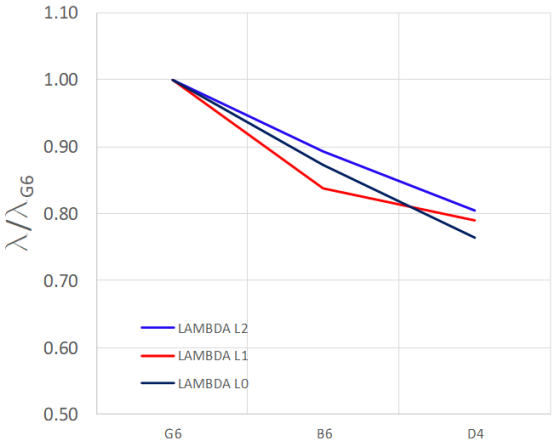

Figure 6.21: Load coefficients for different test points: NES results.

vane. Then the losses cause a reduction of the velocity of the flow at the exit of L0, which in turns reduces the incidence angle in the rotating frame of reference. This is seen in the L0B plot in Figure 6.22, where the L0B pressure distribution for the NES and ES differ mainly at the leading edge. This same behaviour is present in Figure 6.23 for the D4 test point: in this case, however, the nucleation occurs on the L1 rotating blade while the incidence is reduced on the L0 vane. It is also important to observe that most of the effects are present only on the nucleating bladerow and in the one next to it. In fact, the pressure distributions on the L0 blade obtained with the ES and the NES methodologies are almost the same. This confirms the fact that the supercooling disappears just after the nucleation onset and the thermodynamic equilibrium is established between the droplets and the vapour.

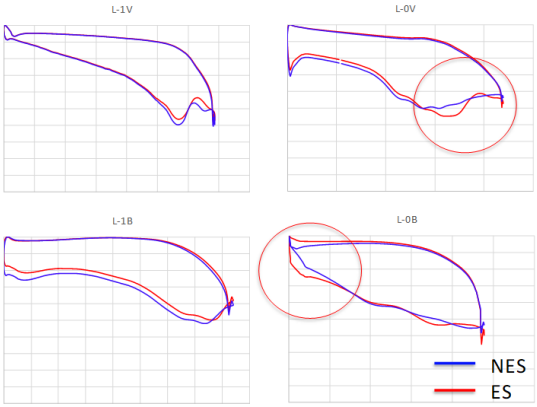

Figure 6.22: Pressure distributions for L1 and L0 stages: B6 test point.

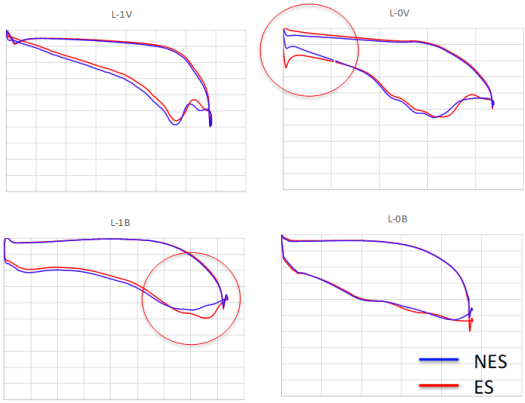

Figure 6.23: Pressure distributions for L1 and L0 stages: D4 test point.

6.4.4 THE COMPARISON WITH THE CORRELATIONS

The numerical results obtained so far shows that a significant improvement in the performance predictability can be achieved by using the NES methodology. For low wetness cases, the results in the previous chapter suggest that when close to the nucleation region the mismatch between ES and NES results is larger, but also that the it is limited to a few blade rows, and its effect vanishes downstream. Of course, as the steam turbines are operated also with moisture level higher than the ones here considered, a caveat must be stated that these conclusions hold only for cases with low wetness. Therefore, a wider range of operating conditions would be required for a better assessment of the NES methodology. In order to show the loss mechanism associated with the nucleation, the equation presented by Gyarmathy [23] is used. As done in the previous section 5.2 for the nucleating steam case, the nucleation losses are evaluated using Equation 5.1 under the assumption that the equilibrium moisture Y_{eq} quoted in the original equation Equation 2.45 is equal to the exit moisture Y_{out}. In order to extract from the CFD results the value of the nucleation losses, the NES cases are compared with their corresponding ES cases by using the outlet-to-inlet growth of entropy, expressed in non-dimensional form $\Delta s/c_p$. The difference between the values of $\Delta s/c_p$ of the NES cases and their corresponding ES cases is shown in Figure 6.24. The comparison in Figure 6.24 show that Equation 5.1 provides a good estimate of the losses associated with the wetness losses, because, in this case, they are mostly due to the nucleation. It is also important to notice that the moisture associated with the nucleation is nearly the same for the stationary vane L0V and

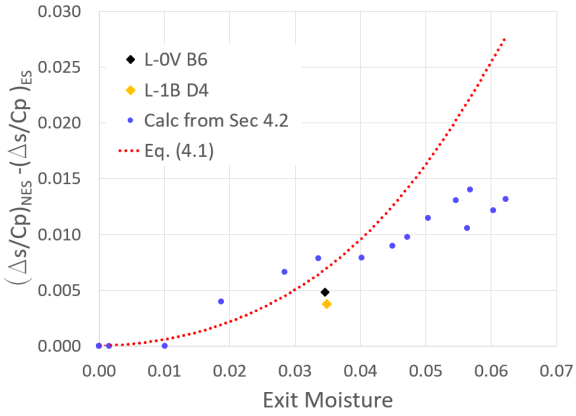

Figure 6.24: Wetness losses: comparison between numerical and theoretical estimates.

the L1B rotating blade, respectively at the B6 and the D4 test point. This is obviously not a general rule, because the results quoted for the Bakhtar cascade in the same plot show that the moisture associated with the nucleation can be higher provided that enough supercooling is present in the steam at the inlet of the bladerow. As for the present case, it is possible to use the results in Figure 6.24 to show that just a few factors account for most of the wetness losses. To do so, the ES expansion lines (A in Figure 6.25) of the points B6 and D4 are divided in a dry and a wet part. The split point, or Wilson point, is assumed to be at an equivalent moisture equal to 3.5%. The starting point of the wet part is then moved according to the nucleation losses obtained from Equation 5.1 (B in Fig. 22). The remaining part of the wet expansion line is finally updated assuming a Baumann factor $\alpha_B = 0.5$, as obtained from Kreitmeier et al. [25] (C in Figure 6.25). The updated expansion lines (D in Figure 6.25) are used to obtain the final efficiency values. The results are shown

in Equation 5.1 in terms of efficiency drop with respect to the G6 test condition. The comparison in Figure 6.26 shows an acceptable agreement between experiments and numerical estimates, which generally confirms that in this case the wetness losses can be estimated using Equation 5.1 with a reasonable accuracy.

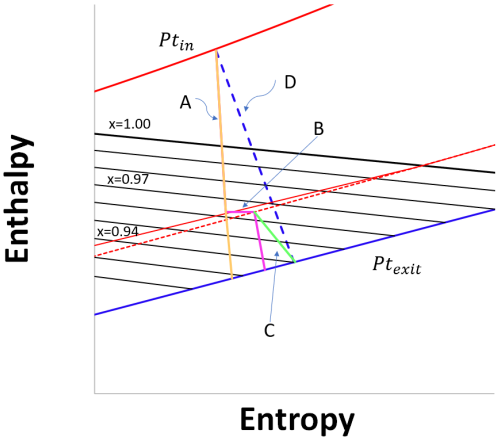

Figure 6.25: Schematic of an expansion line.

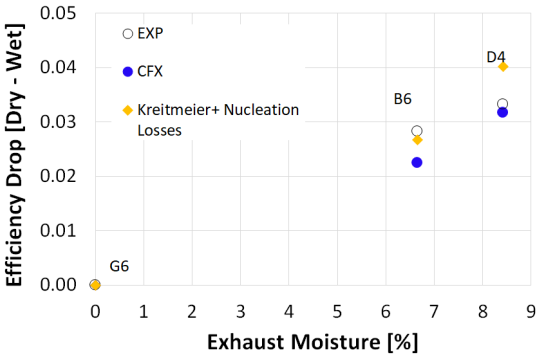

Figure 6.26: Wetness losses: experiments and numerical estimates.

6.4.5 THE KINETIC ENERGY LOSSES

As a last piece of the performance model of the LP section, the numerical results are compared with the correlations used to estimate the correction of the kinetic energy at the LP section exit. In order to do this, the differences between the NES and the ES calculations are calculated for all the considered operating conditions and plotted against the correlations SCC Equation 2.67 and the *Legacy* Equation 2.68 in Figure 6.27. It can be observed that the numerical results do show a significant difference between the NES and ES results. Considering the cases B6 and D4, the LL of the NES calculations are lower than the ES ones. The difference is about 2% at 6% exit moisture and about 2% at 8% of exit moisture for B6 and D4 respectively, which imply a slope between 0.33 and 0.25 of the trend-line. Compared with the correlations, the numerical results range over a wider region of the plot. By considering the point G6, B6 and D4 it is possible to put in evidence that the *Legacy* correlation fits well the data at design condition, with low residual swirl. At the same

time, the way the remaining test points are distributed in the plot show that going from B4 to B9 test points there is a significant effect due to the pressure ratio, or better said, due to the operating condition of the LP section. The SCC correlation Equation 2.67 fits the points at high Mach number but it's very far from the results at low swirl. None of the two correlations fit the complete range, and both are far from the results obtained at the low load B4. The different contributors to the LL reduction can be obtained from the details of the results, through the equation below, derived from Equation 2.66 and adapted to the present case by adding the term LL_L for the residual kinetic energy of the droplets:

$$\frac{LL_{ES} - LL_{NES}}{LL_{ES}} = Y_{ES} + 2\left(\frac{1}{T_{sat}} - \frac{c_p}{L}\right)\Delta T + \\ - 2\frac{(Y)^{ES} - (\hat{Y})^{NES}}{1 - (Y)^{ES}} - Y_{ES}\frac{LL_L}{LL_{ES}} \quad (6.5)$$

Considering, for example, the B9 case, the residual supercooling at the exit of the last stage bucket, is in the order of $4K$, which accounts for a LL reduction of about 2%. The difference in the end points of the expansion lines of the NES and ES cases accounts for another 3% of LL reduction. The remaining part of the LL reduction is due to the significant slip between the droplets and the vapour, which is visible from the Figure 6.28, where the radial distributions of the circumferentially averaged absolute velocities of the two phases are shown. Therefore, predicting the final correction of the exit kinetic energy is difficult due to the complex interaction between these three effects, which is the final reason for the significant inaccuracies obtained from the usage of simple correlations like the SCC and the *Legacy*.

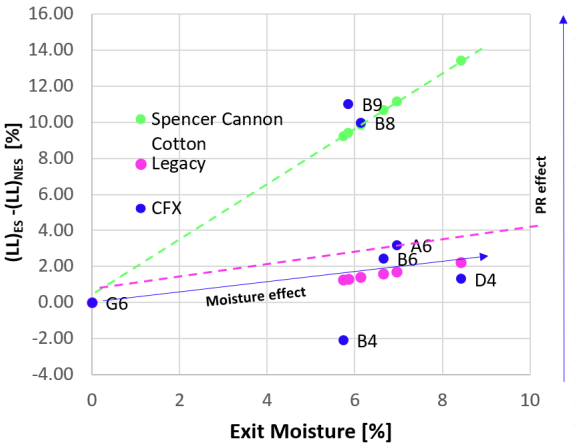

Figure 6.27: Leaving losses: difference between ES and NES results.

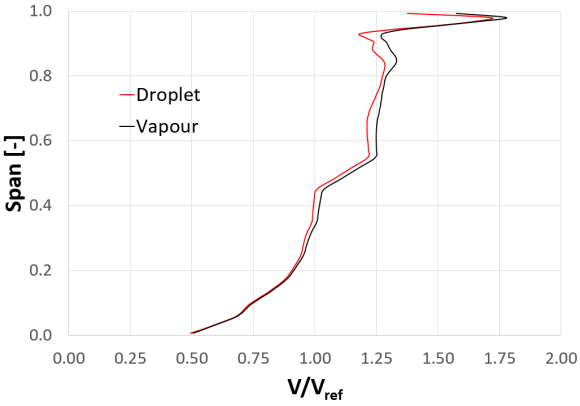

Figure 6.28: Radial distribution of the absolute velocity at the L0 Bucket exit.

Chapter 7

Conclusions

In the OEM's practice, the complexity of the fluid-dynamics in a low pressure steam turbine is managed by combining standard CFD methods with correlations from open literature or built using proprietary data. However, this approach adds some uncertainty in terms of performance and does not provide the pieces of information needed to assess the mechanical robustness of a new design. Therefore, it is always necessary to carry out a significant amount of experimental activity after the development of a new low pressure section, with a consequent investment in terms of time and resources. The purpose of the research presented here is the introduction of the advanced CFD methodologies in the industrial practice to predict the performance and to model the operating conditions of the stages of the LP steam turbines. To do this, a set of user defined functions has been developed to be used in conjunction with a commercial code and tested in a range of configurations and operating conditions.

In chapter 2, the theory behind such development has been shown, and in particular the equations used to model the nu-

cleation of the droplets and their growth have been discussed. As one of the pieces of the current practice is the correlative approach to estimate the wetness losses, the rationale behind some correlations is explained, trying to show clearly the different mechanisms that generate the losses when water droplets nucleate and grow.

In chapter 4, the results obtained by using the new methodology have been presented for some test cases representing plane nozzles, for which experimental data are available from open literature. The obtained results have shown that significant differences exist between the available formulations. Namely speaking, the results obtained for the test case of Moses et al. [39] and Binnie et al. [40] using the formulation developed in Young et al. [16] have been shown to provide an accurate estimate of the droplet size. As an additional advantage over the formulation of Gyarmathy [21], the results have shown to reproduce the experimental data without the need of tuning the model case by case.

Following this first series of results, in chapter 5 the activity has been extended to the analysis of the tip section of a rotor blade of a steam turbine. The analyses discussed in subsection 5.1.1 pertain to cases with supercooled steam at the inlet with subsequent nucleation of droplets described in Bakhtar et al. [42]. The results in subsection 5.1.2 regard the cases without nucleation and droplet steam at the inlet of the cascade, described in Bakhtar et al. [44]. Given the conclusions of the previous activity on plane nozzles, only the methodology from Young et al. [16] has been used. Some adjustments have been applied to improve the agreement between the numerical results and the experimental data: a 20% of increase of the surface tension coefficient and sort of try and error tweaking of the exit

boundary conditions which do not undermine the fact that with this methodology the trend of the losses due to the wetness are well in agreement with the experimental data. In fact, it turns out that a significant uncertainty exists in the experiments because of the transient facility used to produce the supercooled and the wet steam at the cascade inlet.

The CFD results have been also compared with some correlations available from open literature or built on proprietary data. In both the cases, it has been shown that the correlations do a good job only if a posterior information is given about the mechanism behind the wetness losses, because the key parameter to switch from a dry to a nucleating or a droplet laden flow is the amount of maximum supercooling achievable before the nucleation, which in turns depends heavily by the presence and size of droplets at the inlet of the cascade. This means that, in general, the correlations available are "incomplete" compared with the CFD methodology.

Finally, looking for a confirmation of this, in chapter 6 a LP section of recent design has been analysed using the newly developed methodology. The analysis has been performed over a wide range of operating conditions, showing that a good agreement can be achieved using the new approach. Compared with the other considered approaches, with different degree of combination between correlations and CFD, a significant improvement in the predictability has been achieved, in the order of 2 or 3 points of efficiency. The presented results have demonstrated that, in addition to this improvement, the interaction between the droplets and the stage aerodynamics can be correctly accounted for with the newly developed methodology because it considers the real behaviour of the steam. Therefore, such a methodology enables the designer to establish the correct trade-

off between the available options during the design of a new LP section. This has been shown not only for the blading performance, but also for the kinetic energy at the exit of the last stage blade, which is another important piece of the performance model of an LP section.

The performed activity has focused on some operating conditions with limited level of wetness, for which experimental data are available. In this respect however, the presented methodology should be developed in the future, in order to include the effects of the deposition and the detachment of the large droplets from the blade walls. This would provide the designers some very useful pieces of information about the conditions where the LP section stages operate, especially from the point of view of the erosion risk to which the rotating blades are subject. As far as the thermodynamic performance are concerned, however, cases with higher levels of wetness would not present major difficulties, because the large droplets coming from the interaction between the flow and the solid surfaces have a small effect, as they represent a very small fraction of the droplets population.

Therefore, in the vision of the author, CFD represents nowadays an exceptional tool for the prediction of the performance of a steam turbine LP section and for its design. By including the effects of the steam condensation and their interaction with the stage aerodynamics, the developed methodology allows for a significant improvement in predictability compared with the usage of correlations, and the presented results show that virtual testing of LP section with complex hardware can be performed with a good accuracy. Thus, it is foreseen that using the developed methodology will allow to design the next generation of LP sections with higher efficiency, reduced development costs and greater confidence in the performance.

Bibliography

[1] IEA (International Energy Agency. *Global Energy & CO2 Status Report 2018*. OECD/IEA, Paris, France, 2019.

[2] M. Hoznedl, K. Sedlak, L. Mrozek, T. Dadakova, Z. Kubin, and K. Gregor. Experimental and Numerical Study of Flow and Dynamics on LSB at 34 MW Steam Turbine. In *Proceedings of the ASME 2020 Turbo Expo*, volume 7, June 2020.

[3] A. Mambro, F. Congiu, and E. Galloni. CFD Modelling of Steam Turbine Last Stage Blades at Low Load using Multiple Mixing Plane Approach. In *Proceedings of the ASME 2020 Turbo Expo*, volume 7, June 2020.

[4] M. Seiler, V. Zuch, P. Dumstorff, and Almstedt H. Competitive Bidding by Surrogate Modeling of Steam Parameter Influence on the Attainable Start Numbers of Turbine Casings. In *Proceedings of the ASME 2020 Turbo Expo*, volume 7, June 2020.

[5] G. Girezzi, F. Bucciarelli, and D. Checcacci. Steam Turbine Improved Operation and Maintenance by Thermal Warming System. In *Proceedings of the ASME 2020 Turbo Expo*, volume 7, June 2020.

[6] F. Bucciarelli, D. Checcacci, G. Girezzi, and A. Signorini. Operation and Maintenance Improvements of Steam Turbines Subject to Frequent Start by Rotor Stress Monitoring. In *Proceedings of the ASME 2020 Turbo Expo*, volume 7, June 2020.

[7] K. Baumann. Some recent developments in large steam turbine practice. *Journal of the Institution of Electrical Engineersi*, 59(302):565–623, 1921.

[8] G. Gyarmathy. On the design limits of steam turbine last stages. In *Technology of turbine plant operating with wet steam*, pages 55–63. BNES, London, 1988.

[9] Said Havakechian and John Denton. Three-Dimensional Blade-Stacking Strategies and Understanding of Flow Physics in Low-Pressure Steam Turbines—Part I: Three-Dimensional Stacking Mechanisms. *Journal of Engineering for Gas Turbines and Power*, 138(5), 11 2015. 052603.

[10] L.D. Willey, J.R. Maughan, J.M. Hill, and D.J. Walsh. New steam turbine test vehicle for the verification of improved efficiency power generation steam turbines. In *Proceedings of IMECE-2000*, Orlando, FL, Nov 2000. ASME.

[11] L. Cosi, J. Slepski, S. DeLessio, M. Taviani, and A. Mujezinovic. Design, manufacturing and testing of a new family of steam turbine low pressure stages. In *Proceedings of the ASME 2007 Power Conference*, pages 313–320, San Antonio, Texas, USA, July 2007. ASME.

[12] J. Starzmann, F.R. Hughes, S. Schuster, A.J. White, J. Halama, and V. Hric. Results of the international wet steam

modeling project. In *Proceedings of the Institution of Mechanical Engineers: Part A*, volume 232(5), pages 550–570. Journal of Power and Energy, July 2018.

[13] G. Gyarmathy. *Foundations of a Theory of the Wet-Steam Turbine*. OH: Translation Division, Foreign Technology Division, rev. ed. wright patterson air force base edition, 1966.

[14] James E. McDonald. Homogeneous nucleation of vapor condensation. i. thermodynamic aspects. *American Journal of Physics*, 30(12):870–877, 1962.

[15] James E. McDonald. Homogeneous nucleation of vapor condensation. ii. kinetic aspects. *American Journal of Physics*, 31(1):31–41, 1963.

[16] J.B. Young and F. Bakhtar. Non-equilibrium effects in wet-steam turbines. In *Technology of turbine plant operating with wet steam*, Lecture Series. VKI, London, 1980.

[17] Arthur Kantrowitz. Nucleation in very rapid vapor expansions. *The Journal of Chemical Physics*, 19(9):1097–1100, 1951.

[18] F. Bakhtar, J. B. Young, A. J. White, and D.A. Simpson. Classical nucleation theory and its application to condensing steam flow calculations. *Proceedings of the Institution of Mechanical Engineers, Part C: Journal of Mechanical Engineering Science*, 219(12):1315–1333, 2005.

[19] Philip G. Hill. Condensation of water vapour during supersonic expansion in nozzles. *Journal of Fluid Mechanics*, 25(3):593–620, 1966.

[20] W. E. Ranz and W. R. Marshall. Evaporation from drops. *Chem. Eng. Prog.*, 48(3):141–146, 1952.

[21] G. Gyarmathy. The spherical droplet in gaseous carrier streams: Review and synthesis. *Multiphase Science and Technology*, 1(1-4):99–279, 1982.

[22] J.B. Young. The spontaneous condensation of steam in supersonic nozzles. *Physico Chemical Hydrodynamics:PCH*, 3(1):57–82, 1982.

[23] G.Gyarmathy. Basic notions. In M. J. Moore and C. Sieverding, editors, *Two-phase steam flow in turbines and separators : theory, instrumentation, engineering*, pages 31–35. Hemisphere Pub. Corp., Washington, NY, 1976.

[24] J.B. Young. Semi-analytical techniques for investigating thermal non-equilibrium effects in wet steam turbines. *International Journal of Heat and Fluid Flow*, 5(2):81 – 91, 1984.

[25] F. Kreitmeier, R. Greim, F. Congiu, and J. Faelling. Experimental and numerical analyses of relaxation processes in lp steam turbines. *Proceedings of the Institution of Mechanical Engineers, Part C: Journal of Mechanical Engineering Science*, 219(12):1411–1436, 2005.

[26] J. Starzmann, M. Casey, and F. Sieverding. Non-Equilibrium Condensation Effects on the Flow Field and the Performance of a Low Pressure Steam Turbine. In *Proceedings of the ASME 2010 Turbo Expo*, volume 7, pages 2199–2208, June 2010.

[27] EH Miller and P Schofield. The performance of large steam turbine generators with water reactors. In *ASME Winter Meeting*, 1972.

[28] R.C. Spencer and E.H. Miller. Performance of large nuclear turbines. *Journal of Combustion*, 45(2):24 – 30, 1973.

[29] R. C. Spencer, K. C. Cotton, and C. N. Cannon. A Method for Predicting the Performance of Steam Turbine-Generators....: 16,500 kw and Larger. *Journal of Engineering for Power*, 85(4):249–298, 10 1963.

[30] Mamoru Ishii and Takashi Hibiki. *Thermo-Fluid Dynamics of Two-Phase Flow*. 2011.

[31] J.O. Hinze and JO HINZE. *Turbulence*. McGraw-Hill classic textbook reissue series. McGraw-Hill, 1975.

[32] A.J. White and J.B. Young. Loss measurements and interpretation of pitot pressures in two-phase vapor-droplet flow. *Experimental Thermal and Fluid Science*, 15(3):279–287, 1997. Two-Phase Flow.

[33] C. C. Yeoh and J. B. Young. Nonequilibrium Streamline Curvature Throughflow Calculations in Wet Steam Turbines. *Journal of Engineering for Power*, 104(2):489–496, 04 1982.

[34] F. Bakhtar and M.T. Mohammadi Tochai. An investigation of two-dimensional flows of nucleating and wet steam by the time-marching method. *International Journal of Heat and Fluid Flow*, 2(1):5–18, 1980.

[35] A. J. White and J. B. Young. Time-marching method for the prediction of two-dimensional, unsteadyflows of condensing steam. *Journal of Propulsion and Power*, 9(4):579–587, 1993.

[36] A. Liberson, K. Kosolapov, N. Rieger, and S.A. Hesler. Calculation of 3D condensing flows in nozzles and turbine

stages. In *Proceedings of EPRI Nucleation Workshop*, pages 9–1,9–20, June 1995.

[37] A.G. Gerber and M.J. Kermani. A pressure based eulerian–eulerian multi-phase model for non-equilibrium condensation in transonic steam flow. *International Journal of Heat and Mass Transfer*, 47(10):2217 – 2231, 2004.

[38] L. Schiller and Z. Naumann. Ueber die grundlegenden berechnungen bei der schwerkraft-aufbereitung. *Z. Vereines Deutscher Inge.*, 77:318–321, 1933.

[39] C. A. Moses and G. D. Stein. On the Growth of Steam Droplets Formed in a Laval Nozzle Using Both Static Pressure and Light Scattering Measurements. *Journal of Fluids Engineering*, 100(3):311–322, 09 1978.

[40] A. M. Binnie, J. R. Green, and R. V. Southwell. An electrical detector of condensation in high-velocity steam. *Proceedings of the Royal Society of London. Series A. Mathematical and Physical Sciences*, 181(985):134–154, 1942.

[41] Jörg Starzmann, Fiona R. Hughes, Alexander J. White, Marius Grübel, and Damian M. Vogt. Numerical Investigation of Boundary Layers in Wet Steam Nozzles. *Journal of Engineering for Gas Turbines and Power*, 139(1), 09 2016. 012606.

[42] F. Bakhtar, M . Ebrahimi, and R. A. Webb. On the performance of a cascade of turbine rotor tip section blading in nucleating steam: Part 1: Surface pressure distributions. *Proceedings of the Institution of Mechanical Engineers, Part C: Journal of Mechanical Engineering Science*, 209(2):115–124, 1995.

[43] F.Bakhtar, M.Ebrahimi, and B.O.Bamkole. On the performance of a cascade of turbine rotor tip section blading in nucleating steam: Part 2: Wake traverses. *Proceedings of the Institution of Mechanical Engineers, Part C: Journal of Mechanical Engineering Science*, 209(3):169–177, 1995.

[44] F. Bakhtar, H. Mashmoushy, and O. C. Jadayel. On the performance of a cascade of turbine rotor tip section blading in wet steam part 2: Surface pressure distributions. *Proceedings of the Institution of Mechanical Engineers, Part C: Journal of Mechanical Engineering Science*, 211(7):531–540, 1997.

[45] M.J. Kermani and A.G. Gerber. A general formula for the evaluation of thermodynamic and aerodynamic losses in nucleating steam flow. *International Journal of Heat and Mass Transfer*, 46(17):3265 – 3278, 2003.

[46] Jörg Starzmann, Michael M Casey, Jürgen F Mayer, and Frank Sieverding. Wetness loss prediction for a low pressure steam turbine using computational fluid dynamics. *Proceedings of the Institution of Mechanical Engineers, Part A: Journal of Power and Energy*, 228(2):216–231, 2014.

[47] Marius Grübel, Markus Schatz, and Damian M. Vogt. Second Law Analysis of Condensing Steam Flows. In *Proceedings of the ASME 2018 Turbo Expo*, volume 8, 06 2018. V008T29A025.

[48] T. Guo, W. J. Sumner, and D. C. Hofer. Development of Highly Efficient Nuclear HP Steam Turbines Using Physics Based Moisture Loss Models. In *Proceedings of the ASME 2007 Turbo Expo*, volume 6, pages 825–833, 05 2007.

[49] Markus Häfele, Christoph Traxinger, Marius Grübel, Markus Schatz, Damian M. Vogt, and Roman Drozdowski. Experimental and Numerical Investigation of the Flow in a Low-Pressure Industrial Steam Turbine With Part-Span Connectors. *Journal of Engineering for Gas Turbines and Power*, 138(7), 02 2016. 072604.

[50] Hiteshkumar Mistry, Manisekaran Santhanakrishnan, John Liu, Alexander Stein, Subhrajit Dey, and Jonathon Slepski. Aerodynamic Performance Assessment of Part-Span Connector of Last Stage Bucket of Low Pressure Steam Turbine. In *Proceedings of the ASME 2011 Power Conference*, volume 1, pages 545–550, 07 2011.

[51] E. Ferhatoglu, S. Zucca, D. Botto, J. Auciello, and L. Arcangeli. Nonlinear Vibration Analysis of Turbine Bladed Disks With Mid-Span Dampers. In *Proceedings of the ASME 2020 Turbo Expo*, volume 7, June 2020.

[52] Sai S. Sreedharan, Hiteshkumar Mistry, Vsevolod Ostrovskiy, and Tao Guo. Performance Evaluation of Last Stage Bucket Tip Section Using Non-Equilibrium Wet Steam CFD Tool. In *Proceedings of ASME 2015 Turbo Expo: Power for Land, Sea, and Air*, volume 8, 06 2015. V008T26A038.

[53] Tommaso Diurno, Tommaso Fondelli, Leonardo Nettis, Nicola Maceli, Lorenzo Arcangeli, Antonio Andreini, and Bruno Facchini. Numerical Investigation on the Aerodynamic Performance of a Low-Pressure Steam Turbine Exhaust Hood Using Design of Experiment Analysis. *Journal of Engineering for Gas Turbines and Power*, 142(11), 10 2020. 111006.

[54] J. Young and A. White. Editorial. *Proceedings of the Institution of Mechanical Engineers, Part A: Journal of Power and Energy*, 228(2):108–109, 2014.

[55] Shigeki Senoo, Takeshi Kudo, Hisataka Fukushima, Kiyoshi Segawa, and Kazuya Sakakibara. Development and Verification Tests of Titanium 50-Inch and 60-Inch Last Stage Blades for Steam Turbines. In *Proceedings of ASME 2019 Turbo Expo: Power for Land, Sea, and Air*, volume 8, 06 2019. V008T29A001.

[56] Ondrej Novak, Marek Bobcik, Vaclav Slama, Bartolomej Rudas, Josef Kellner, Petr Mestanek, Jan Hlous, Zdenek Simka, Martin Luxa, David Simurda, Antonin Zivny, Ales Macalka, and Jiri Ira. Development of Highly Efficient and Robust Ultra-Long Last Stage Blade for High Backpressure. In *Proceedings of ASME 2019 Turbo Expo: Power for Land, Sea, and Air*, volume 8, 06 2019. V008T29A007.

[57] O. Brunn, U. Harbecke, T. Mokulys, V. Salit, M.A. Schwarz, and F. Dornbusch. Improved LP-Stage Design for Industrial Steam Turbines. In *Proceedings of the ASME 2020 Turbo Expo*, volume 7, June 2020.

[58] John Basirico, Bin Zhou, Amir Mujezinovic, Yuri Starodubtsev, and Boris Frolov. Testing of Full Speed No Load Operating Conditions in a Subscale Steam Turbine Test Vehicle. In *Proceedings of ASME 2011 Turbo Expo: Power for Land, Sea, and Air*, volume 7, pages 2455–2461, 06 2011.

[59] Francesco Piraccini, Roberto Biondi, and Lorenzo Cosi. Aeromechanic Validation of a New Steam Turbine LP Section: Test Major Outcomes. In *Proceedings of ASME 2010*

Turbo Expo: Power for Land, Sea, and Air, volume 6, pages 819–826, 06 2010.

[60] N. Maceli, S. Della Gatta, S. Lorusso, V. Michelassi, T. Jurek, T. Watkins, and J. Slepski. Investigating a new family of lp steam turbines: test results and post-test analyses. In *Technology Insights*, pages 149–156. Nuovo Pignone, Firenze, Italia, 2011.

[61] J. Bellucci, L. Peruzzi, A. Arnone, L. Arcangeli, and N. Maceli. Numerical and Experimental Aerodynamic Investigation of a Low Pressure Steam Turbine Module. In *Proceedings of ASME 2019 Turbo Expo: Power for Land, Sea, and Air*, volume 8, 06 2019. V008T29A024.

[62] A. M. Wallis, J. D. Denton, and A. A. J. Demargne. The Control of Shroud Leakage Flows to Reduce Aerodynamic Losses in a Low Aspect Ratio, Shrouded Axial Flow Turbine. *Journal of Turbomachinery*, 123(2):334–341, 02 2000.

[63] A. Pfau, A. I. Kalfas, and R. S. Abhari. Making Use of Labyrinth Interaction Flow. *Journal of Turbomachinery*, 129(1):164–174, 03 2004.

[64] B. Rosic, J.D. Denton, and E.M. Curtis. The Influence of Shroud and Cavity Geometry on Turbine Performance: An Experimental and Computational Study—Part I: Shroud Geometry. *Journal of Turbomachinery*, 130(4), 06 2008. 041001.

[65] J. B. Young. Critical Conditions and the Choking Mass Flow Rate in Nonequilibrium Wet Steam Flows. *Journal of Fluids Engineering*, 106(4):452–458, 12 1984.